Appendix 2

Key Formulas in Earthquake Seismology

Yehuda Ben-Zion
University of Southern California, Los Angeles, California, USA

Introduction

The material below contains selective key formulas for different branches of earthquake seismology, with an emphasis on source processes, accompanied by brief explanations. The goal is to provide a concise collection of useful expressions in one place without elaborate background information and details. The formulas are organized in seven brief sections: 1. *Thermodynamics and elastodynamics*; 2. *Seismic source and representation integrals*; 3. *Elastodynamic waves*; 4. *Fracture*; 5. *Friction*; 6. *Earthquake source parameters and scaling relations*; and 7. *Seismicity patterns.* The choice and ordering of material is to some extent a matter of taste (and of course knowledge). Most formulas are followed only by definitions and basic clarifications, but in some places there is also a brief discussion of properties and implications of results. Further details on the different subjects, and many additional important formulas, can be found in the references given by numbers in the parentheses after the title of each section. Since most expressions are well-known, explicit references are usually not provided for each separate result; however, in some cases this is done for easy identification of sources. An excellent general reference for the material of sections 1, 2, 3, and 6 is the book *Quantitative Seismology* by Aki and Richards [1]. Good general references for sections 4 and 5 in relation to earthquakes are Rice [42] and Scholz [50]. Useful general references for section 6 are Brune and Thatcher [8] and Kanamori [25]. A good general reference for section 7 is Utsu [59].

The following notations are adopted throughout. Variables and parameters are written in italics (e.g., x), vectors are denoted with boldface (e.g., $\boldsymbol{x}$), and unit vectors are marked with the circumflex symbol (e.g., $\hat{\boldsymbol{n}}$). Cartesian components of vectors and tensors are denoted with subscripts (e.g., x_i, c_{ijkl}). The summation convention for repeating subscripts is used (e.g., $c_{ijkl}\varepsilon_{kl} = \sum_{k,l} c_{ijkl}\varepsilon_{kl}$). Overdots indicate time derivatives (e.g., $\ddot{u}_i = \partial^2 u_i/\partial t^2$), and a comma after a subscript implies a spatial derivative (e.g., $\sigma_{ij,j} = \sum_j \partial\sigma_{ij}/\partial x_j$). Additional notations are defined where needed.

1. Thermodynamics and Elastodynamics ([1], [37], [43], [55], [57])

The first law of thermodynamics implies that the energy balance during evolving deformation can be expressed as

$$d\Omega/dt + dQ/dt = d(K+U)/dt \tag{1.1}$$

where Ω, Q, K, and U are, respectively, mechanical work, heat, kinetic energy, and internal energy, all per unit mass or volume. The internal energy is an intrinsic potential such as gravity, magnetic field, and elastic strain energy. If the internal energy is known as a function of strain ε and entropy $\mathcal{S}$, it forms a complete equation of state, and all other equilibrium properties of a deforming system, such as specific heat and stress–strain relation, can be obtained from it by differentiation. For some applications, it is preferable to use the strain and temperature T as independent variables. In that case, the complete equation of state is given by the Helmholtz free energy F defined as

$$F = U - T\mathcal{S} \tag{1.2}$$

where F, U, and $\mathcal{S}$ are per unit mass or volume.

The second law of thermodynamics requires that the entropy production rate during any process in a closed system be nonnegative

$$d\mathcal{S} \geq 0 \tag{1.3}$$

INTERNATIONAL HANDBOOK OF EARTHQUAKE AND ENGINEERING SEISMOLOGY, VOLUME 81B ISBN: 0-12-440658-0

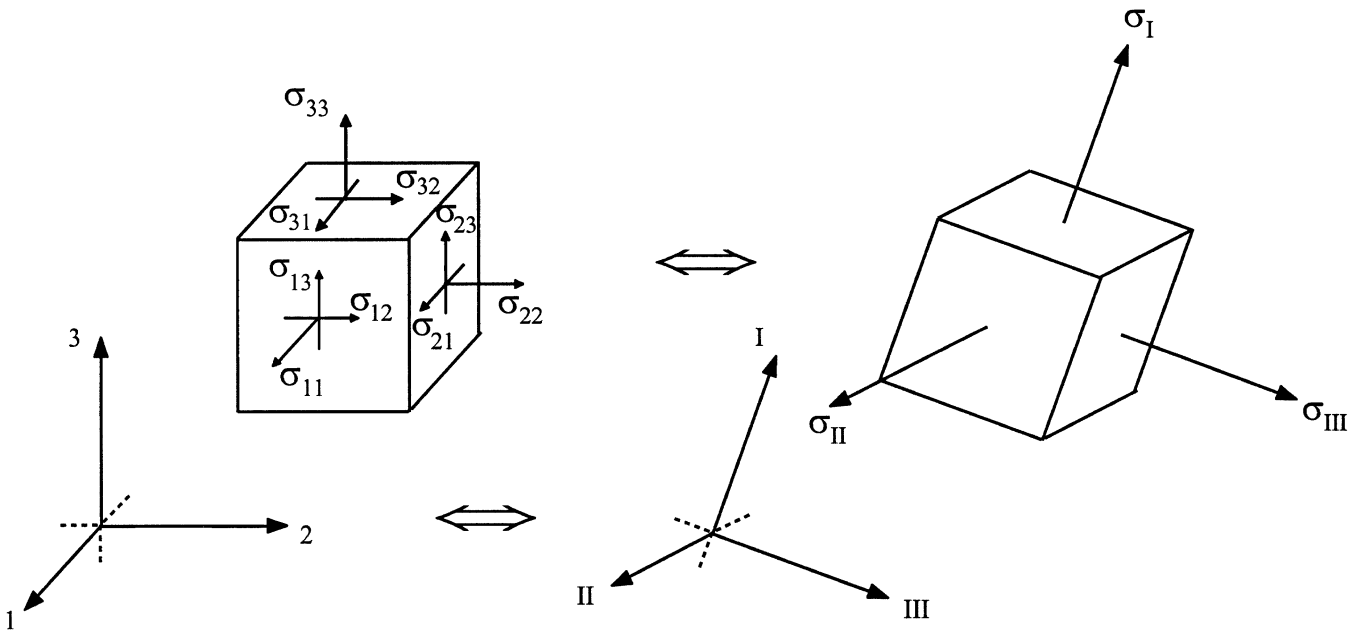

FIGURE 1 The stress tensor in a general coordinate system having nine shear and normal components (left) and the principal coordinate system having only three normal components (right).

with the equality characterizing reversible processes (e.g., purely elastic deformation) and the ">" sign characterizing irreversible ones (e.g., fracture and friction).

The stress tensor σ_{ij} and moduli tensor c_{ijkl} of elastic deformation can be obtained from the strain energy density function W and strain tensor ε_{ij} by the following derivatives

$$\sigma_{ij} = \rho' \partial W / \partial \varepsilon_{ij} \tag{1.4a}$$

and

$$c_{ijkl} = \partial^2 W / \partial \varepsilon_{ij} \partial \varepsilon_{kl} \tag{1.4b}$$

where ρ' is mass density if W is energy density per unit mass or 1 if it is energy density per unit volume. For deformation under adiabatic conditions, the appropriate choice for W is U, while for isothermal deformation it is F.

The stress–strain relation of a linear elastic solid is

$$\sigma_{ij} = c_{ijkl} \varepsilon_{kl}. \tag{1.4c}$$

The stress, strain, and elastic moduli tensors have the following symmetry properties

$$\begin{aligned} &\sigma_{ij} = \sigma_{ji}, \\ &\varepsilon_{ij} = \varepsilon_{ji}, \\ &c_{ijkl} = c_{jikl} = c_{ijlk} = c_{klij}. \end{aligned} \tag{1.4d}$$

With the above definitions and properties, the strain energy density per unit volume of a linear elastic solid is

$$W = \frac{1}{2} c_{ijkl} \varepsilon_{ij} \varepsilon_{kl} = \frac{1}{2} \sigma_{ij} \varepsilon_{ij}. \tag{1.4e}$$

Since the stress and strain tensors are symmetric and real-valued, they can always be diagonalized by transformation (Fig. 1) to a coordinate system consisting of three orthogonal directions (called the principal axes) normal to planes subjected only to normal stress and strain components (called the principal stress and strain values).

The stress–strain relation for a linear isotropic elastic solid is

$$\sigma_{ij} = \lambda \delta_{ij} \varepsilon_{kk} + 2\mu \varepsilon_{ij} \tag{1.5}$$

where λ and μ are the Lamé constants and δ_{ij} is the Kronecker delta function. The Lamé constants and bulk modulus K can be written in terms of Young modulus E and Poisson ratio ν as

$$\begin{aligned} &\mu = E/[2(1+\nu)], \\ &\lambda = \nu E/[(1+\nu)(1-2\nu)], \\ &K = E/[3(1-2\nu)] = \lambda + 2\mu/3. \end{aligned} \tag{1.6}$$

For a uniaxial linear elastic deformation of homogeneous isotropic bar under tensile stress σ_{11}, the axial strain components are $\varepsilon_{11} = \sigma_{11}/E$, $\varepsilon_{22} = \varepsilon_{33} = -\nu \varepsilon_{11}$ and the shear strain components are zero. During infinitesimal deformation of homogeneous isotropic elastic solid under pressure $-p$, the normal stress components are $\sigma_{11} = \sigma_{22} = \sigma_{33} = -p$ and the fractional reduction of volume is $\Delta V/V = (\varepsilon_{11} + \varepsilon_{22} + \varepsilon_{33}) = -p/K$.

The Cauchy equation of motion for a continuum in terms of stress and displacement $\boldsymbol{u}$ is

$$\sigma_{ij,j} + f_i = \rho \ddot{u}_i \tag{1.7}$$

where f_i is the i component of body force per unit volume.

Putting (1.5) into (1.7), and using the definition of infinitesimal strain in terms of displacement gradients $\varepsilon_{ij} = \frac{1}{2}(u_{i,j}+u_{j,i})$, gives the Navier equation of motion for a linear homogeneous isotropic elastic solid in terms of infinitesimal displacement

$$(\lambda + \mu)u_{k,ki} + \mu u_{i,kk} + f_i = \rho \ddot{u}_i. \tag{1.8}$$

Equation (1.8) has solutions in a homogeneous medium in terms of two types of plane body waves $\boldsymbol{u}(\boldsymbol{x}, t) = \hat{\boldsymbol{p}}u(\hat{\boldsymbol{n}} \cdot \boldsymbol{x} - ct)$, consisting of an arbitrary pulse shape u propagating in direction $\hat{\boldsymbol{n}}$ with velocity c and particle motion polarization $\hat{\boldsymbol{p}}$. One solution has velocity and polarization

$$c = v_P \equiv \sqrt{(\lambda + 2\mu)/\rho} \quad \text{and} \quad \hat{\boldsymbol{p}} \times \hat{\boldsymbol{n}} = 0 \tag{1.9a}$$

and the other

$$c = v_S \equiv \sqrt{\mu/\rho} \quad \text{and} \quad \hat{\boldsymbol{p}} \cdot \hat{\boldsymbol{n}} = 0. \tag{1.9b}$$

Solutions (1.9a) and (1.9b) describe longitudinal dilatational P waves and transverse shear S waves, respectively. More general wavefields can be represented as superpositions of plane waves (see section 3).

The strain energy density per unit volume of a plane S or P wave in a linear isotropic elastic solid is

$$W = \frac{1}{2}\sigma_{ij}\varepsilon_{ij} = \frac{1}{2}\rho \dot{u}^2 = K \tag{1.9c}$$

where K is the kinetic energy density per unit volume. The flux rate of energy transmission (i.e., energy per unit time across a unit area normal to the propagation direction) associated with a plane wave of elastic disturbance is $v_S \rho \dot{u}^2$ for S waves and $v_P \rho \dot{u}^2$ for P waves.

The displacement field generated by a distribution of body forces and surface tractions can be synthesized using the elastodynamic Green function $G_{ij}(\boldsymbol{x}, t; \boldsymbol{x}', t')$, giving the i component of displacement at $(\boldsymbol{x}, t)$ due to a localized unit body force operating at $(\boldsymbol{x}', t')$ in the j direction. The elastodynamic Green function satisfies the Navier equation of motion for a linear elastic solid

$$\rho \frac{\partial^2}{\partial t^2} G_{ij} = \delta_{ij}\delta(\boldsymbol{x} - \boldsymbol{x}')\delta(t - t') + \frac{\partial}{\partial x_n}(c_{inkl}\frac{\partial}{\partial x_l}G_{kj}) \tag{1.10}$$

where $\delta(\ )$ is the Dirac delta function. A complete determination of G_{ij} requires meeting initial conditions (taken usually to be $G = \partial G/\partial t = 0$ for $t \le t'$ and $\boldsymbol{x} \ne \boldsymbol{x}'$) and specified boundary conditions on the surface of the medium.

If G_{ij} satisfies homogeneous boundary conditions (i.e., zero traction or zero displacement) on S, it has the following spatiotemporal reciprocity properties

$$G_{ij}(\boldsymbol{x}, t; \boldsymbol{x}', t') = G_{ji}(\boldsymbol{x}', -t'; \boldsymbol{x}, -t). \tag{1.11}$$

The displacement field in a solid with volume V and surface S subjected to body force $\boldsymbol{f}$ and surface traction $\boldsymbol{T}$ can be written using a Green function response that satisfies stress-free boundary conditions on S as

$$u_i(\boldsymbol{x}, t) = \int_{-\infty}^{t} dt' \int_V G_{ij}(\boldsymbol{x}, t; \boldsymbol{x}', t')\, f_j(\boldsymbol{x}', t')\, d^3\boldsymbol{x}' + \int_{-\infty}^{t} dt' \int_S G_{ij}(\boldsymbol{x}, t; \boldsymbol{x}', t')\, T_j(\boldsymbol{x}', t')\, d^2\boldsymbol{x}'. \tag{1.12}$$

2. Seismic Source and Representation Integrals

([1], [3], [4], [12], [21], [28], [34], [42], [57])

The total strain at $(\boldsymbol{x}, t)$ may be written as a sum of elastic and inelastic contributions (Fig. 2). The inelastic strain tensor in the faulting region, also called transformational strain, defines the seismic potency density tensor per unit volume,

$$\varepsilon^P_{ij}(\boldsymbol{x}, t) \equiv \text{ seismic potency density tensor.} \tag{2.1a}$$

The corresponding transformational stress, also called stress glut, defines the seismic moment density tensor per unit volume,

$$c_{ijkl}(\boldsymbol{x})\varepsilon^P_{kl}(\boldsymbol{x}, t) \equiv m_{ij}(\boldsymbol{x}, t) \equiv \text{ seismic moment density tensor.} \tag{2.1b}$$

Relation (2.1b) assumes that the tensor of elastic moduli is time-invariant. Since this does not hold during faulting, c_{ijkl} should be interpreted as a tensor of "effective" elastic constants with actual employed values depending on the application. If ε^P_{kl} is identified as the tensor of elastic strain drop during faulting, m_{ij} may be interpreted as the corresponding stress drop tensor $\Delta\sigma_{ij}$,

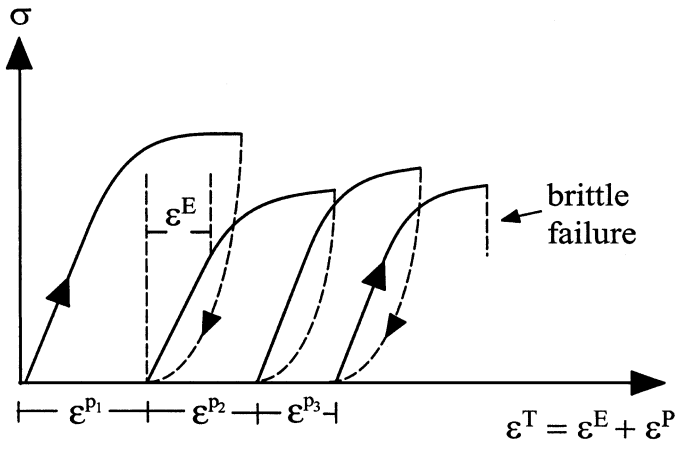

FIGURE 2 A schematic 1-D stress–strain diagram for large deformation with total strain ε^{T} having elastic ε^{E} and inelastic ε^{P} contributions.

and c_{ijkl} as effective elastic constants relating the elastic strain drop tensor to the stress drop tensor.

The seismic potency tensor is

$$P_{ij}(t) = \int_V \varepsilon_{ij}^P \, dV \tag{2.2a}$$

where the integral covers the inelastically deforming volume in the earthquake source region. Similarly, the seismic moment tensor is

$$M_{ij}(t) = \int_V c_{ijkl} \, \varepsilon_{kl}^P \, dV = \int_V \Delta\sigma_{ij} \, dV. \tag{2.2b}$$

For a displacement discontinuity $\Delta \boldsymbol{u}$ across a surface S with a unit normal $\hat{\boldsymbol{n}}$

$$P_{ij}(t) = \frac{1}{2} \int_S (\Delta u_i n_j + \Delta u_j n_i) \, dS \tag{2.3a}$$

and

$$M_{ij}(t) = \int_S c_{ijkl} \Delta u_k n_l \, dS. \tag{2.3b}$$

For isotropic material

$$M_{ij}(t) = \int_S [\lambda \delta_{ij} \Delta u_k n_k + \mu(\Delta u_j n_i + \Delta u_i n_j)] \, dS. \tag{2.3c}$$

The scalar seismic potency of shear faulting on a planar surface is the integral of slip over the rupture area or, equivalently, the product of the spatial average of the final slip distribution and the failure area A

$$P_0 = \langle \Delta u \rangle \, A. \tag{2.4a}$$

The corresponding scalar seismic moment is

$$M_0 = \mu P_0 = \mu \, \langle \Delta u \rangle \, A \tag{2.4b}$$

with μ being an effective rigidity in the source area.

The displacement field at $(\boldsymbol{x}, t)$ due to a distribution of m_{jk} $(= c_{pqjk} n_q \Delta u_p)$ along an internal surface S is

$$u_i(\boldsymbol{x}, t) = \int_{-\infty}^{t} dt' \int_S c_{pqjk}(\boldsymbol{x}') n_q(\boldsymbol{x}') \Delta u_p(\boldsymbol{x}', t') \times [\partial G_{ij}(\boldsymbol{x}, t; \boldsymbol{x}', t')/\partial x_k'] \, d^2x'. \tag{2.5a}$$

The displacement field at $(\boldsymbol{x}, t)$ due to a distribution of displacement discontinuities along an internal surface S can be written as

$$u_i(\boldsymbol{x}, t) = \int_{-\infty}^{t} dt' \int_S \Delta u_j(\boldsymbol{x}', t') B_{ij}(\boldsymbol{x}, t; \boldsymbol{x}', t', \hat{\boldsymbol{n}}) \, d^2x' \tag{2.5b}$$

where B_{ij} gives the i component of displacement at $(\boldsymbol{x}, t)$ due to a unit point dislocation in the j direction at $(\boldsymbol{x}', t')$ across a surface S with a unit normal $\hat{\boldsymbol{n}}(\boldsymbol{x}')$. The situation $\hat{\boldsymbol{e}}_j \cdot \hat{\boldsymbol{n}} = 0$ with $\hat{\boldsymbol{e}}_j$ being a unit vector in the j direction corresponds to a shear crack, while $\hat{\boldsymbol{e}}_j \times \hat{\boldsymbol{n}} = 0$ represents a tensile crack. For shear faulting in isotropic material

$$B_{ij}(\boldsymbol{x}, t; \boldsymbol{x}', t', \hat{\boldsymbol{n}}) = n_k \mu [\partial G_{ij}(\boldsymbol{x}, t; \boldsymbol{x}', t')/\partial x_k' + \partial G_{ik}(\boldsymbol{x}, t; \boldsymbol{x}', t')/\partial x_j']. \tag{2.5c}$$

For 2-D static crack problems, the stress drop and spatial derivative of slip are proportional to the Hilbert transforms of each other. For example, the stress drop sustained by a crack on the plane $x_2 = 0$ in a region $[-L, L]$ along the x_1 axis due to a slip distribution in that region is

$$\Delta\sigma_{2j}(x_1, x_2 = 0) = \frac{\mu}{2\pi(1-\nu)} \times \int_{-L}^{L} \frac{d[\Delta u_j(x_1') - \nu \delta_{j3} \Delta u_3(x_1')]/dx_1'}{x_1 - x_1'} \, dx_1' \tag{2.6}$$

where $j = 1$ and 3 correspond to in-plane and antiplane shear, respectively, and $j = 2$ corresponds to opening motion. Relation (2.6) stems from the fact that a line dislocation at $x_1 = x_1'$ produces stresses that decay with distance r from the source like $1/r$.

3. Elastodynamic Waves

([1], [10], [12], [30], [33], [42], [49], [51], [57], [61], [64])

As mentioned in section 1, the Navier equation of motion for a linear elastic solid has solutions in terms of P and S plane body waves and elastodynamic Green functions. Stress-free surfaces, interfaces separating solids with different elastic properties, and other heterogeneities produce reflected/transmitted/converted waves and additional seismic phases. A solid with a free surface, taken to be horizontal, is referred to as a half space. Shear waves with horizontal polarization in an isotropic half space or horizontally layered structures, called *SH* waves, excite on horizontal planes a single stress component (e.g., σ_{zy} for a coordinate system with z normal to horizontal planes and y in the polarization direction). Corresponding S waves with vertical polarization, called *SV* waves, excite on horizontal planes the other two components of stress (e.g., σ_{zx} and σ_{zz}). Incident *SH* waves produce upon interaction with horizontal interfaces only *SH* reflected/transmitted waves, while *SV* (and also P) waves interacting with horizontal interfaces produce in general both *SV* and P reflected/transmitted waves.

Rayleigh waves consist of combined P and SV elastic disturbances propagating along a free surface of elastic solid. For a Poissonian half space, having $\lambda = \mu$ and $\nu = 0.25$, the Rayleigh wave velocity is $v_R \approx 0.92 v_S$. In a half space with increasing v_S and v_P with depth, or a corresponding spherical situation, Rayleigh waves are dispersive. In such cases, the longer wavelength components are affected by deeper structure and, hence, propagate faster. Love waves are dispersive SH waves that travel, again with faster propagation for longer wavelength components, within a horizontal surface layer or the top section of a half space having increasing v_S with depth (or corresponding situations with spherical geometry). Stoneley waves are combined P and SV disturbances propagating along an interface between pairs of solids with elastic properties in a certain range or between a solid and a fluid.

Plane waves form a complete set of basis functions and, hence, can be used to represent any wavefield. In practice, they are useful in problems with geometrical elements that are naturally characterized by a Cartesian geometry (e.g., planar surfaces on which boundary conditions should be satisfied), and in high-frequency seismology with propagation distance much larger than the wavelength. Other complete sets of basis functions that are commonly used in wave propagation seismology are Bessel/Hankel functions and spherical harmonics. Bessel and Hankel functions are useful in problems with elements that have a cylindrical or spherical geometry (e.g., 2-D problems with a line source, 3-D problems with a point source, tunnel or borehole in a 3-D solid). Spherical harmonics provide a natural representation for the angular dependency of normal modes (free oscillations) of the Earth and are useful in other problems of low-frequency seismology (e.g., surface waves). The radial dependency of normal modes is described by spherical Bessel functions. In a spherically symmetric solid, there are two distinct types of normal modes, toroidal and spheroidal. Toroidal modes are analogous to SH and Love waves and are associated only with an angular motion. Spheroidal modes are analogous to P/SV and Rayleigh waves and are associated with both radial and angular motion.

The elastodynamic Green function in an unbounded homogeneous isotropic solid has P and S wave components

$$G_{ij}(\boldsymbol{x}, \boldsymbol{x}', t) = G_{ij}^P + G_{ij}^S \tag{3.1a}$$

where

$$G_{ij}^P = -(\partial^2/\partial x_i \partial x_j)\, h(r, t; v_P) \tag{3.1b}$$

and

$$G_{ij}^S = -(\delta_{ij}\nabla^2 - \partial^2/\partial x_i \partial x_j)\, h(r, t; v_S) \tag{3.1c}$$

with (Fig. 3)

$$h(r, t; c) = -\frac{1}{4\pi\rho r}(t - r/c)\, H(t - r/c). \tag{3.1d}$$

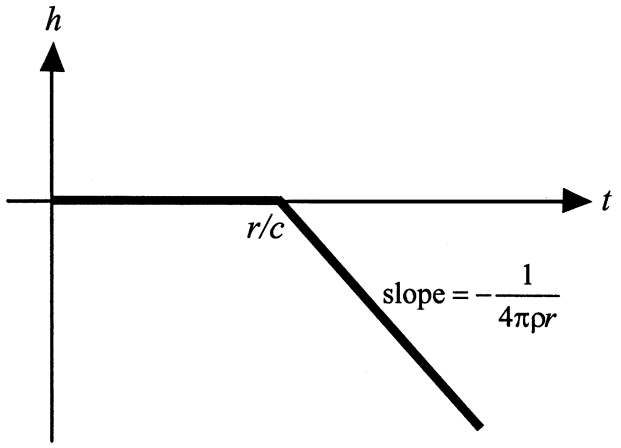

FIGURE 3 The function $h(r, t; c)$ at space-time distances (r, t) from a source in a solid with wave velocity c.

In (3.1b)–(3.1d), the source operates at zero time, r is the source-receiver distance, v_P and v_S are P and S wave velocities, and H is the Heaviside unit step function.

The elastodynamic Green functions for 2- and 3-D homogeneous isotropic solids can be written in the frequency domain [61] as

$$G_{ij}(\boldsymbol{x}, \boldsymbol{x}', \omega) = \frac{1}{4\pi\rho\omega^2}\left\{\delta_{ij}k_S^2 g(k_S r) - \frac{\partial}{\partial x_i}\frac{\partial}{\partial x_j}[g(k_P r) - g(k_S r)]\right\} \tag{3.2}$$

where ω is angular frequency, $k_S = \omega/v_S$, $k_P = \omega/v_P$, $g(kr) = \exp(-ikr)/r$ for a 3-D solid, and $g(kr) = i\pi H_0(kr)$ for a 2-D case with H_0 being the Hankel function of order zero.

The displacement field in an unbounded homogeneous isotropic material generated by a distribution of m_{jk} can be written from (2.5) and (3.1) as

$$u_i(\boldsymbol{x}, t) = u_i^P + u_i^S \tag{3.3a}$$

where

$$u_i^{P\,or\,S}(\boldsymbol{x}, t) = O_{ijk}^{P\,or\,S} \int_V \int_{-\infty}^{t} h(r, t - t'; v_{P\,or\,S}) \times m_{jk}(\boldsymbol{x}', t')\, dt'\, d^3x' \tag{3.3b}$$

with

$$O_{ijk}^P = \partial^3/\partial x_i \partial x_j \partial x_k \tag{3.3c}$$

and

$$O_{ijk}^S = \frac{1}{2}(\delta_{ij}\partial/\partial x_k + \delta_{ik}\partial/\partial x_j)\nabla^2 - \partial^3/\partial x_i \partial x_j \partial x_k. \tag{3.3d}$$

The far-field approximation of (3.3a)–(3.3d), valid for $r \gg a$ and $r \gg \lambda$ with a and λ being source dimension and wavelength of interest, is

$$u_i^{PorS}(\boldsymbol{x}, t) = \frac{R_{ijk}^{PorS}}{4\pi\rho r_0 v_{PorS}^3} \int_V \dot{m}_{jk}\left(\boldsymbol{x}', t - \frac{r_0 - \gamma_i x_i'}{v_{PorS}}\right) d^3x' \tag{3.4a}$$

where r_0 is a representative source-receiver distance, $\gamma_i = \partial r/\partial x_i = x_i/r$ are components of the unit vector in the source-receiver direction, the integral term is referred to as source effect, and the receiver plus radiation pattern functions R in front of the integral are

$$R_{ijk}^P = \gamma_i\gamma_j\gamma_k \tag{3.4b}$$

and

$$R_{ijk}^S = \frac{1}{2}(\delta_{ij}\gamma_k + \delta_{ik}\gamma_j) - \gamma_i\gamma_j\gamma_k. \tag{3.4c}$$

The γ_i terms in (3.4b) and (3.4c) are associated with the variable of interest at the receiver, while the other terms are associated with radiation patterns for P and S waves.

For a unidirectional slip in the x_1 direction on a fault surface in the x_1-x_3 plane (Fig. 4), the corresponding far-field displacement field is

$$u_i^{PorS}(\boldsymbol{x}, t) = \frac{R_{i12}^{PorS} v_S^2}{2\pi r_0 v_{PorS}^3} \int_S \Delta\dot{u}_1[x_1', x_3', t + (\gamma_1 x_1' + \gamma_3 x_3' - r_0)/v_{PorS}]\, d^2x'. \tag{3.5a}$$

The factor $1/r_0$ in (3.4a) and (3.5a) accounts for the geometric attenuation of body waves in the far-field. The ratio of the maximum amplitudes of far-field displacement S waves to P waves is essentially v_P^3/v_S^3, which is about 5 for a Poissonian solid. Denoting the source effect (integral term) in (3.5a) by $\Omega(\boldsymbol{x}', t)$, the zero-frequency asymptote of the far-field displacement source spectrum is

$$\Omega(\boldsymbol{x}', \omega = 0) = \int_S d^2x' \int_{-\infty}^{\infty} \Delta\dot{u}_1\, dt = \int_S \Delta u_1(\boldsymbol{x}', t = T_r)\, d^2x' = \langle\Delta u_1\rangle A = P_0 \tag{3.5b}$$

where T_r is the time at the completion of the dynamic slip process (called the rise time), $\langle\Delta u_1\rangle$ is the spatial average of slip over the fault, A is the rupture area, and P_0 is the scalar seismic potency (see section 2). The zero-frequency asymptote of the far-field spectrum of any plausible description of the source process is equal to the scalar seismic potency or moment divided by rigidity (see, e.g., equation (3.8) and Fig. 7). Details of different source processes are contained in the high-frequency portions of the spectra.

The far-field condition $r \gg \lambda$ is equivalent to a high-frequency criterion $|\omega| \gg v_{SorP}/r$. Thus (3.4) and (3.5) do not represent properly the low-frequency components of the fields radiated from distributions of slip and moment density tensors. In particular, these results do not include the final static components of the response. Equations (3.4) and (3.5) have approximate descriptions of space-time variations of the source process (viewed from a constant source-receiver angle and without terms that attenuate faster than $1/r$). In contrast, point-source and low-frequency approximations of the far-field radiation from a distribution of m_{jk} are associated with more limiting conditions at the source. The point-source approximation is valid for $\lambda \gg a$ and $r \gg \lambda$, and the corresponding results do not include spatial variations at the source. The low-frequency approximation is valid for $|\omega|T_r \ll 1$ and $r \gg \lambda$, and the corresponding results do not include space or time variations of the source process.

The complete displacement field in an unbounded homogeneous isotropic material due to a spatially localized body force with a source-time function $\boldsymbol{F}(t)$ is

$$u_i(\boldsymbol{x}, t) = \frac{1}{4\pi\rho}(3\gamma_i\gamma_j - \delta_{ij})\frac{1}{r^3}\int_{r/v_P}^{r/v_S} \tau F_j(t - \tau)\, d\tau + \frac{1}{4\pi\rho v_P^2}\gamma_i\gamma_j\frac{1}{r}F_j(t - r/v_P) - \frac{1}{4\pi\rho v_S^2}(\gamma_i\gamma_j - \delta_{ij})\frac{1}{r}F_j(t - r/v_S). \tag{3.6}$$

The first term with unseparated P and S waves decays with distance like $1/r^2$ for sources that are nonzero for times shorter than the interval $(r/v_S - r/v_P)$. Since this term is dominant for very short source-receiver distances ($r \to 0$), it is called the near-field term. The second and third terms with separate P and S wave contributions proportional to $1/r$ are dominant at large distances ($r \to \infty$) and are called far-field terms.

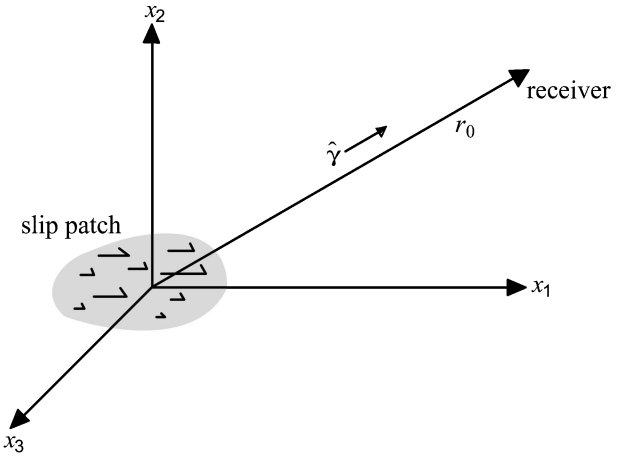

FIGURE 4 A coordinate system for analysis of far-field radiation at receiver with distance r_0 and angle $\hat{\boldsymbol{\gamma}}$ from a fault with unidirectional slip $\Delta\boldsymbol{u} = [\Delta u_1(x_1, x_3, t), 0, 0]$.

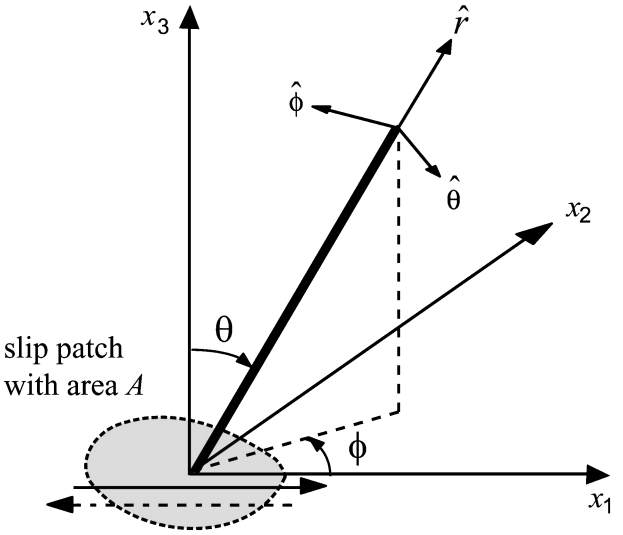

FIGURE 5 Cartesian and polar coordinate systems for analysis of radiation by a slip patch with area A and average slip $\langle \Delta u(t) \rangle$.

The corresponding displacement field generated by a time-dependent scalar seismic moment $M_0(t) = \mu \langle \Delta u(t) \rangle A$, associated with a shear dislocation (Fig. 5) parallel to a fault surface with an area A, is

$$\begin{aligned} \boldsymbol{u}(\boldsymbol{x}, t) = {} & \frac{1}{4\pi\rho} \boldsymbol{A}^N \frac{1}{r^4} \int_{r/v_P}^{r/v_S} \tau M_0(t-\tau)\, d\tau \\ & + \frac{1}{4\pi\rho v_P^2} \boldsymbol{A}^{IP} \frac{1}{r^2} M_0(t - r/v_P) \\ & + \frac{1}{4\pi\rho v_S^2} \boldsymbol{A}^{IS} \frac{1}{r^2} M_0(t - r/v_S) \\ & + \frac{1}{4\pi\rho v_P^3} \boldsymbol{A}^{FP} \frac{1}{r} \dot{M}_0(t - r/v_P) \\ & + \frac{1}{4\pi\rho v_S^3} \boldsymbol{A}^{FS} \frac{1}{r} \dot{M}_0(t - r/v_S). \end{aligned} \tag{3.7a}$$

The first term in (3.7a) with unseparated P and S waves gives the near-field response, the second and third terms with separate P- and S-wave contributions proportional to $1/r^2$ are intermediate-field terms, and the fourth and fifth terms with separate P and S waves proportional to $1/r$ are the far-field terms. The functions $\boldsymbol{A}$ in front of each term are radiation patterns for the various terms given by

$$\begin{aligned} \boldsymbol{A}^N &= 9 \sin 2\theta \cos\phi \hat{\boldsymbol{r}} - 6(\cos 2\theta \cos\phi \hat{\boldsymbol{\theta}} - \cos\theta \sin\phi \hat{\boldsymbol{\phi}}), \\ \boldsymbol{A}^{IP} &= 4 \sin 2\theta \cos\phi \hat{\boldsymbol{r}} - 2(\cos 2\theta \cos\phi \hat{\boldsymbol{\theta}} - \cos\theta \sin\phi \hat{\boldsymbol{\phi}}), \\ \boldsymbol{A}^{IS} &= -3 \sin 2\theta \cos\phi \hat{\boldsymbol{r}} + 3(\cos 2\theta \cos\phi \hat{\boldsymbol{\theta}} - \cos\theta \sin\phi \hat{\boldsymbol{\phi}}), \\ \boldsymbol{A}^{FP} &= \sin 2\theta \cos\phi \hat{\boldsymbol{r}}, \\ \boldsymbol{A}^{FS} &= \cos 2\theta \cos\phi \hat{\boldsymbol{\theta}} - \cos\theta \sin\phi \hat{\boldsymbol{\phi}}, \end{aligned} \tag{3.7b}$$

where $\hat{\boldsymbol{r}}$, $\hat{\boldsymbol{\theta}}$, and $\hat{\boldsymbol{\phi}}$ are unit direction vectors in a polar coordinate system for the source-receiver geometry (Fig. 5). The far-field radiation patterns provide the basis for routine derivation of fault-plane solutions from observed spatial distributions of first-motion polarities.

The largest amplitude arrivals at teleseismic distances are surface Rayleigh and Love waves, which attenuate with distance like $r^{-1/2}$ in contrast to the r^{-1} attenuation of body waves. For this reason, surface waves are used extensively to derive information from observed seismograms on low-frequency properties of earthquake sources and the velocity structure of the crust and upper mantle.

The far-field displacement amplitude spectrum from a unidirectional rupture on a rectangular fault with length L, width $W \ll L$, rupture velocity V_r in the positive length direction, and ramp source-time function with final slip D and rise time T_r is

$$|\Omega(\boldsymbol{x}, \omega)| = WLD \frac{\sin X}{X} \left| \frac{1 - e^{i\omega T}}{\omega T_r} \right| \tag{3.8}$$

where $X = (\omega L/2)[1/V_r - (\cos\Psi)/v_{P\text{or}S}]$ and Ψ is the angle between the rupture direction and receiver. The function $\sin X/X$, called the finiteness factor or directivity function, accounts for the finite apparent rupture duration at different directions and produces oscillations with nodes at $X = \pi, 2\pi, \ldots$. The term in the square bracket of X times L gives the apparent rupture duration at receiver direction Ψ (Fig. 6). The zero-frequency asymptote of (3.8), WLD, is the scalar seismic potency (see also (3.5b) and section 2), while at high frequencies (3.8) is a decaying oscillatory function with a high-frequency asymptote proportional to ω^{-2}.

In general, the low-frequency asymptote of the far-field displacement source spectrum, being independent of internal variations of the source process, is a stable constant value equal to the scalar potency or moment divided by rigidity. In contrast, the high-frequency spectral source behavior depends strongly on model assumptions and parameters. Kinematic rupture models that start from a point and spread with a uniform velocity to prescribed boundaries have far-field displacement spectra with high-frequency asymptotes proportional to ω^{-2}–ω^{-3} for most model assumptions and source-receiver directions (Fig. 7). The frequency at the intersection of the low- and high-frequency asymptotes is called the corner frequency ω_c. For source models with uniform rupture propagation over a continuous fault in a full space, ω_c is inversely proportional to the rupture dimension. However, the precise value of ω_c depends strongly on details of the source process, source-receiver direction, and wave type (P or S).

The attenuation of elastic strain energy during a stress cycle with angular frequency ω may be characterized in terms of a quality factor $Q(\omega)$ as

$$\frac{1}{Q(\omega)} = -\frac{\Delta E}{2\pi E} \tag{3.9a}$$

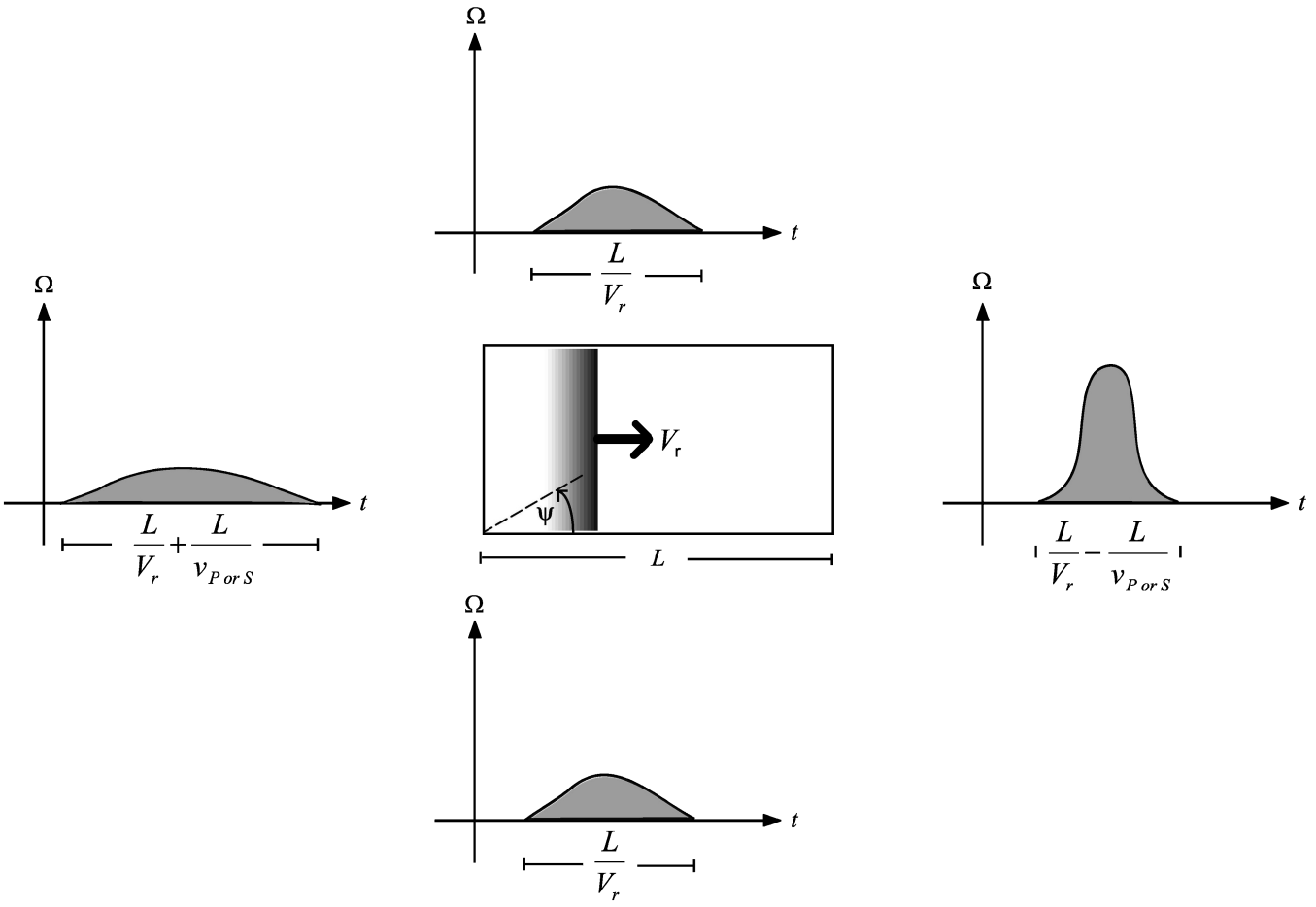

FIGURE 6 A schematic representation of displacement pulses $\Omega(t)$ radiated at different directions from a propagating rupture. The areas under the curves are the same, but the amplitudes and durations are different.

where E and ΔE are the peak and change of elastic strain energy during the cycle. An effective way of incorporating attenuation into solutions of elastic wave propagation problems, when Q is approximately constant over a wide range of frequencies, is to multiply the elastic body-wave velocities by the function

$$[1 + \ln(\omega/\omega_0)/\pi Q - i/2Q] \tag{3.9b}$$

where ω_0 is a reference angular frequency (e.g., 2π) for which the body-wave phase velocities are known and i is the imaginary unit.

The amplitude response $|X(\omega)|$ and phase delay $\phi(\omega)$ of a pendulum seismometer with mass M, spring constant k, and dashpot constant D are given by

$$|X(\omega)| = \frac{\omega^2}{\sqrt{\left(\omega^2 - \omega_s^2\right)^2 + 4\varepsilon^2\omega^2}} \tag{3.10a}$$

and

$$\phi(\omega) = \pi - \tan^{-1}\frac{2\varepsilon\omega}{\omega^2 - \omega_s^2} \tag{3.10b}$$

where $2\varepsilon = D/M, \omega_s = (k/M)^{1/2}$ and the dimensionless damping constant ε/ω_s is equal to half the reciprocal of the Q value of a damped oscillator.

4. Fracture ([5], [7], [15], [17], [28], [29], [31], [32], [42], [44], [46], [47], [50], [54])

Holes, notches, cracks, inclusions, and other flaws in solids amplify or concentrate stress near their boundaries. For example, the tensile stress on the boundary of a circular hole around the origin of the x_1-x_2 plane with remote loading σ^∞ in the x_2 direction is

$$\sigma_{\theta\theta} = \sigma^\infty(1 + 2\cos 2\theta) \tag{4.1}$$

where $\theta = 0$ on the positive x_1 axis. Equation (4.1) indicates a stress concentration by a factor of 3 at the intersections of the hole with the x_1 axis.

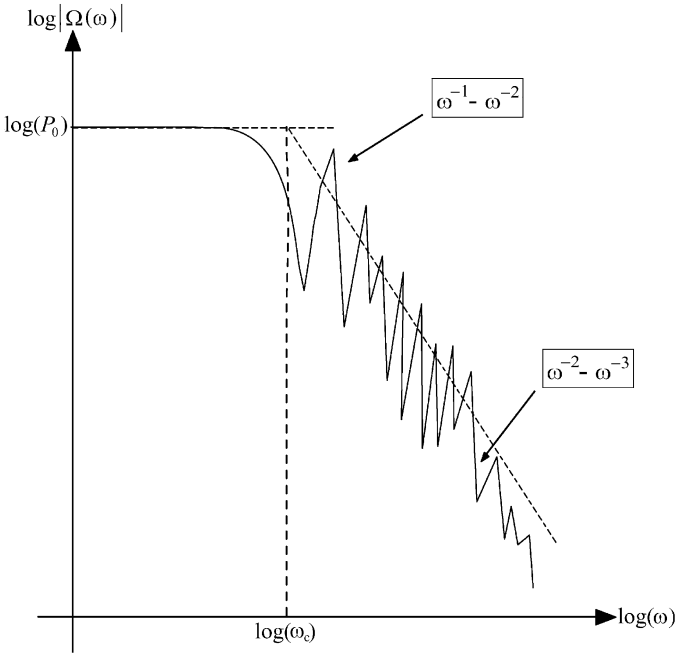

FIGURE 7 A schematic representation of radiated far-field displacement source spectrum with scalar seismic potency P_0 and corner frequency ω_c.

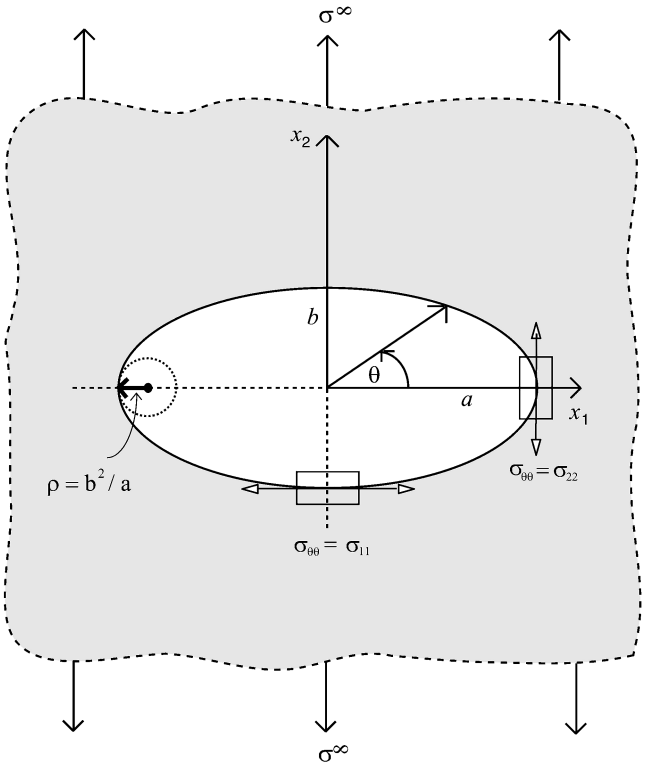

FIGURE 8 An elliptical hole with a radius of curvature ρ in a plate under remote tensile loading σ^∞.

The tensile stress at the x_1 intersections of an elliptical hole (Fig. 8) around the origin of the x_1-x_2 plane with major and minor axes a and b under remote loading σ^∞ in the x_2 direction is

$$\sigma_{\theta\theta}(x_1 = \pm a, x_2 = 0) = \sigma^\infty(1 + 2a/b) = \sigma^\infty(1 + 2\sqrt{a/\rho}) \tag{4.2}$$

where $\rho = (b^2/a)$ is the radius of curvature of the ellipse at $x_1 = \pm a$. The limit $b \to 0$ corresponds to a flat Griffith crack. In that limit, modeled as a sharp mathematical cut, the stress concentration at $x_1 = \pm a$ becomes unbounded. This is a general feature of all problems in Linear Elastic Fracture Mechanics (LEFM), where the breakdown processes at the crack tips are ignored. The region of validity of LEFM is at distances from the crack tip (Fig. 9) larger than the inelastic process zone and much smaller than any macroscopic dimension such as crack length or distances from boundaries. Nonlinear fracture mechanics models incorporate constitutive laws for the inelastic deformation in the process zone that eliminate the crack tip singularities (see, e.g., Fig. 11 for slip-weakening friction behind the rupture front).

For a flat Griffith crack of length $2a$ on the x_1 axis under remote tensile loading σ^∞ in the x_2 direction, the tensile stress along the x_1 axis and slip Δu_2 are

$$\sigma_{22}(|x_1| > a, x_2 = 0) = \sigma^\infty |x_1| / \sqrt{x_1^2 - a^2} \tag{4.3a}$$

and

$$\Delta u_2(|x_1| < a) = (4\sigma^\infty / E')\sqrt{a^2 - x_1^2} \tag{4.3b}$$

where $E' = E$ for plane stress and $E' = E/(1 - \nu^2)$ for plane strain with E and ν being Young modulus and Poisson ratio, respectively. The $1/\sqrt{r}$ and $\sqrt{r'}$ functional dependencies in (4.3a) and (4.3b), with r and r' denoting the distances from the crack tip to points in the unbroken and broken material, respectively, are common to all 2D, 3D, static, dynamic, isotropic, and anisotropic problems in LEFM (Fig. 10).

A useful way of quantifying the strength of the singular crack tip field in LEFM problems is through the limit

$$K = \lim_{r \to 0} \left[\sigma\sqrt{2\pi r}\right] \tag{4.4}$$

where K is called the stress intensity factor.

The singular stress and displacement discontinuity fields along dynamic planar cracks under general mixed loading have the following general forms

$$\{\sigma_{22}, \sigma_{21}, \sigma_{23}\} = \frac{1}{\sqrt{2\pi r}}\{K_{\mathrm{I}}, K_{\mathrm{II}}, K_{\mathrm{III}}\} \tag{4.5a}$$

and

$$\{\Delta u_2, \Delta u_1, \Delta u_3\} = \frac{4(1-\nu)}{\mu} \times \sqrt{\frac{r'}{2\pi}}\{K_{\mathrm{I}} f_{\mathrm{I}}, K_{\mathrm{II}} f_{\mathrm{II}}, K_{\mathrm{III}} f_{\mathrm{III}}/(1-\nu)\}. \tag{4.5b}$$

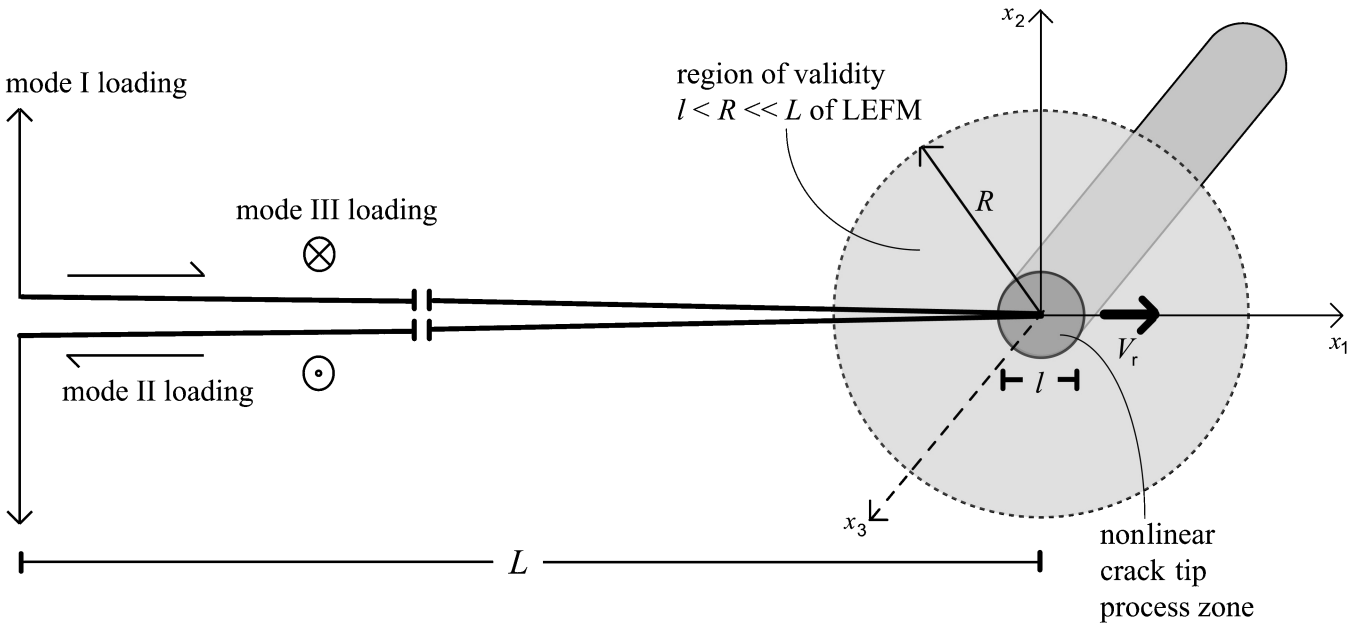

FIGURE 9 A schematic diagram of a 2-D crack illustrating the region of validity of Linear Elastic Fracture Mechanics and modes I, II, and III of rupture extending along the x_1 axis with velocity V_r.

The functions K_J are stress intensity factors for modes J = I, II, and III. A pure mode I corresponds to an "opening" tensile fracture with particle motion normal to the crack surface (Fig. 9). A pure mode II corresponds to a "sliding" in-plane shear fracture with particle motion in the crack plane and parallel to the direction of crack extension. A pure mode III corresponds to a "tear" antiplane shear fracture with particle motion in the crack plane and normal to the direction of crack extension (Fig. 10). For cracks that grow from an initial "nucleation" size with continuing slip behind the propagating front, the functions K_J decrease monotonically with the crack speed to zero: $K_I(V_r \to v_R) \to 0$, $K_{II}(V_r \to v_R) \to 0$, $K_{III}(V_r \to v_S) \to 0$ with v_R and v_S being the Rayleigh and shear wave speeds, respectively. For cracks expanding from the origin at a uniform speed V_r, $K_J \propto \Delta\sigma_J\sqrt{V_r t}$ where $\Delta\sigma_J = \sigma_J^\infty - \sigma_J^{crack}$ are stress drop components associated with the different modes. A static crack of length $2a$ in an infinite plate has $K_J = \sigma_J^\infty\sqrt{\pi a}$. The functions f_J in (4.5b) increase monotonically with the crack speed such that $f_J(V_r = 0) = 1$ for all modes, and $f_I(V_r \to v_R) \to \infty$, $f_{II}(V_r \to v_R) \to \infty$, $f_{III}(V_r \to v_S) \to \infty$. The products $K_J f_J$ governing the amplitudes of the displacement discontinuity fields remain finite. Explicitly,

$$f_I = \frac{\alpha_P V_r^2}{(1-\nu)v_S^2 R}, \quad f_{II} = \frac{\alpha_S V_r^2}{(1-\nu)v_S^2 R}, \quad f_{III} = 1/\alpha_S \quad (4.5c)$$

where $\alpha_P = \sqrt{1 - V_r^2/v_P^2}$, $\alpha_S = \sqrt{1 - V_r^2/v_S^2}$, and $R = 4\alpha_P\alpha_S - (1 + \alpha_S^2)^2$. The Rayleigh function R vanishes when $V_r = v_R$.

Shear fracture in mode II on a frictional interface can propagate at intersonic velocities [46] larger than the above speed limits for singular cracks (v_R for modes I and II; v_S for mode III) and smaller than the dilatational wave speed v_P. The singular solution, not just along a planar extension of the crack as in (4.5a) and (4.5b) but for all positions, includes an angular component that depends on V_r. The full singular solution predicts, for a homogeneous solid, rotations of maximum failure stress components away from the continuation of a planar crack and, hence, branching [15] at certain values of V_r. Branching is expected to be suppressed by high compressive normal stress, and for rupture in a weak layer (e.g., of a damaged fault zone rock) surrounded by a stronger material or along the interface between such a layer and the host solid (or other dynamically weak interfaces).

Inferred values of earthquake rupture velocity averaged over the failure area are usually about 75% of the estimated v_S of the host rock [25, 53]. Such V_r values may exceed the S-wave velocity of the (damaged) fault zone material, which can be considerably lower (e.g., by 25% or more) than that of the host rock. In some cases, there is evidence ([46] and references therein) that V_r exceeds along part of the rupture surface the v_R and v_S velocities of the host rock. Very low values of V_r (e.g., 1% v_S of the host rock or less) are sometimes inferred in association with so-called slow earthquakes (e.g., [22] and references therein).

During a self-similar growth of a circular crack with uniform V_r and $\Delta\sigma$, the slip is

$$\Delta u = [A(V_r)\Delta\sigma/\mu]\sqrt{V_r^2 t^2 - X^2}, \quad (4.6a)$$

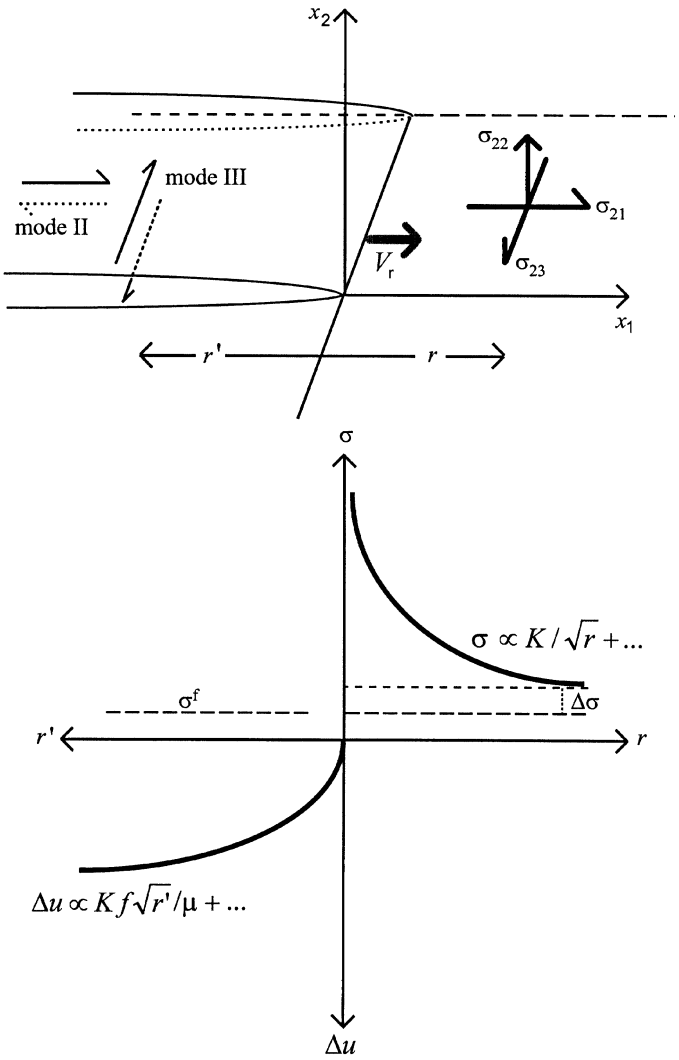

FIGURE 10 Singular stress and displacement fields with intensity factors K and Kf, respectively, for mode II or III shear crack having frictional stress σ^f and stress drop $\Delta\sigma$.

where $A(V_r)$ is of order 1 for $0 \le V_r \le v_R$ and X is the distance from the center of the crack.

The corresponding radiated far-field displacement is proportional to the stress drop

$$u \propto 2\pi A(V_r) V_r^3 t^2 \Delta\sigma/\mu. \tag{4.6b}$$

Equation (4.6b) can be used to estimate the dynamic stress drop from the initial pulse of seismic radiation.

For a crack growing in its plane, the energy release from the crack tip per new unit surface area is

$$G = \left\{(1-\nu)\left(K_{\mathrm{I}}^2 f_{\mathrm{I}} + K_{\mathrm{II}}^2 f_{\mathrm{II}}\right) + K_{\mathrm{III}}^2 f_{\mathrm{III}}\right\}/2\mu. \tag{4.7}$$

The different mode-components of G decrease monotonically with V_r in the subsonic regime, from maximum values at $V_r = 0$ to zero at the limiting speeds.

During a short-time crack extension of distance a with nonuniform velocity $V_r(t)$, prior to arrival back at the advancing tip of wave reflections from the other crack tip or boundaries, the stress intensity factor of a given mode can be written as the product

$$K = K^*(a) K[V_r(t)] \tag{4.8a}$$

where $K^*(a)$ is the "rest" stress intensity factor equal to that of a semi-infinite static crack that advanced the same distance a into the same initial stress field and the non-dimensional function $K[V_r(t)]$ decreases monotonically from unity at $V_r(t) = 0$ to zero at the appropriate limiting speed. Similarly, the corresponding energy release rate can be written as

$$G = G^*(a) G[V_r(t)] \tag{4.8b}$$

with similar interpretations of the terms.

The failure fracture criterion for initiation of rupture in a given mode J = I, II, III is

$$K_{\mathrm{J}} = K_{\mathrm{Jc}} \tag{4.9a}$$

where K_{J} is the appropriate stress intensity factor and K_{Jc} is a corresponding material property called fracture toughness.

The failure fracture criterion for continuation of dynamic rupture propagation is

$$G = G_c \tag{4.9b}$$

where G_c is a material property specifying the amount of energy required for the creation of a unit new surface area. For a purely brittle fracture process associated with the creation of a new surface by a reversible separation of atoms, $G_c = 2\Gamma_{\mathrm{S}}$ with Γ_{S} being the specific Griffith surface energy.

For a 2-D quasi-static crack extending in the x_1 direction, the integral

$$J = \int_{\mathrm{C}} (W n_1 - n_i \sigma_{ij} \partial u_j/\partial x_1)\, dS \tag{4.10}$$

is path-independent for all contours C that begin and end on the crack. In (4.10), n_i are components of the outer unit normal to C and W is the strain energy density $W(\varepsilon) = \int_0^{\varepsilon} \sigma_{ij}\, d\varepsilon_{ij}$.

For frictionless cracks $J = G$, while for cracks that support a frictional stress σ_{2j}^f, $J_Q = G + \sigma_{2j}^f (\Delta u_j)_Q$ with Q being any point on the crack.

5. Friction ([5], [13], [31], [32], [35], [38], [41], [42], [45], [50])

The resistance to initial macroscopic tangential motion along a sliding surface is often described by the Coulomb friction

$$\tau_f = c + f_s \sigma_n \tag{5.1}$$

where c is a cohesion term representing resistance due to joined portions of the surface, f_s is the static coefficient of friction,

and σ_n is normal stress. In cases where pore fluids are present, σ_n should be replaced by $\sigma_n^{effective} = (\sigma_n - p)$ with p being the pore pressure. The same holds for σ_n in all other expressions of this section. In friction experiments with many rock types (not including some clay materials), the data can be fitted by the lines

$$(c = 0,\ f_s = 0.85) \quad \text{for} \quad \sigma_n < 200\ \text{MPa} \tag{5.2a}$$

and

$$(c = 50\ \text{MPa},\ f_s = 0.6) \quad \text{for} \quad 200\ \text{MPa} < \sigma_n < 1700\ \text{MPa} \tag{5.2b}$$

with some scatter representing, at least in part, dependency on surface conditions and rock type. Equation (5.1) with coefficients given by (5.2) is referred to as Byerlee friction.

Equation (5.1) also describes the failure envelope on a Mohr diagram of rock fracturing experiments with $\sigma_n < 1000$ MPa. In that context, f_s is called the coefficient of internal friction, and inferred values of f_s are, as in Byerlee friction, about 0.7. However, values of c in shear fracture experiments are considerably larger than those associated with frictional sliding.

Frictional resistance in which the friction coefficient decreases with slip Δu is referred to as slip-weakening friction (Fig. 11). A simple triangular form often used in numerical calculations is

$$f = f_s - (f_s - f_d)\Delta u / D_c \quad \text{for} \quad \Delta u < D_c \tag{5.3a}$$

and

$$f = f_d \quad \text{for} \quad \Delta u \geq D_c \tag{5.3b}$$

where f_s and f_d are static and dynamic friction coefficients and D_c is a characteristic slip-weakening distance. In the context of the slip-weakening friction (5.3), the fracture energy density per unit fault area associated with the breakdown processes leading to strength degradation (see e.g., Fig. 14a) is

$$G_c = \sigma_n (f_s - f_d) D_c / 2. \tag{5.3c}$$

Values of G_c based on shear laboratory fracture data [31, 41] with various pressure-temperature conditions and rock types, interpreted with slip-weakening friction, are in the range 10^4–10^5 J/m^2. For comparisons, estimates of G_c based on initiation and stopping of earthquakes and modeling of seismic data are in the range 10^6–10^8 J/m^2, estimates of G_c in tensile lab fracture experiments with granite are in the range 3–50 J/m^2, and estimates of the specific Griffith surface energy for various materials are in the range 1–2 J/m^2.

The spatial region behind the tip of the sliding material where the strength degradation occurs and slip achieves a value of D_c (see Fig. 11) is called the process zone, degradation zone, or breakdown zone. The linear size of this region is

$$X_c = c\mu D_c / [\sigma_n (f_s - f_d)] \tag{5.3d}$$

where c is a dimensionless constant of order 2–3 and μ is rigidity. Laboratory values of D_c depend on the roughness of the sliding surface and possible existence of gouge. In experiments done so far [31, 41], it is in the range $(10^{-6} - 5 \times 10^{-4})$ m. Using $f_s - f_d \approx 0.05$ and a representative ratio for the seismogenic zone $\mu/\sigma_n \approx 300$ implies values of X_c in the range $(10^{-2}$–$10)$ m. Implications of the critical weakening distance to nucleation of slip instabilities are discussed below.

Rate- and state-dependent friction laws characterize the dependency of the friction coefficient on slip, slip velocity, history (represented by state variables), and normal stress. In a "standard" form of rate- and state-dependent friction (Fig. 12), with a single state variable θ and no dependency of the friction coefficient on normal stress, the friction coefficient can be written as

$$f = f_0 + a \ln(v/v_0) + b \ln(v_0 \theta / L) \tag{5.4a}$$

where f_0 is a nominal friction coefficient (about 0.7 for most rocks as indicated in (5.2)), v and v_0 are current and reference values of sliding velocity, a is the amplitude of the initial response to a velocity jump, and b is the amplitude of gradual strength alteration over a characteristic slip distance L (also denoted by D_c) following a velocity jump. There are two common versions that describe the evolution of the state variable. In the "slowness" version, the state variable satisfies

$$d\theta/dt = 1 - v\theta/L \tag{5.4b}$$

whereas in the "slip" version

$$d\theta/dt = -(v\theta/L) \ln(v\theta/L). \tag{5.4c}$$

In both cases, during steady-state sliding with constant velocity and slip distance larger than L, $\theta = L/V$ and the steady-state dependency of the friction coefficient on the sliding velocity is

$$f_{ss} = f_0 + (a - b) \ln(v/v_0). \tag{5.4d}$$

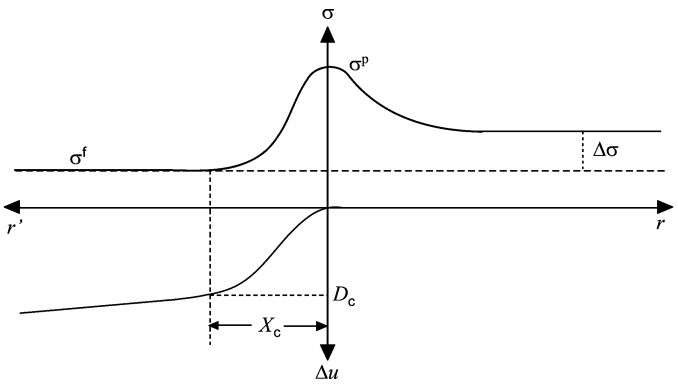

FIGURE 11 A schematic diagram of slip-weakening friction with strength $\sigma(\Delta u)$ decaying from a peak value σ^p to a residual level σ^f over a characteristic slip distance D_c. The sizes of the breakdown zone and stress drop are X_c and $\Delta\sigma$, respectively.

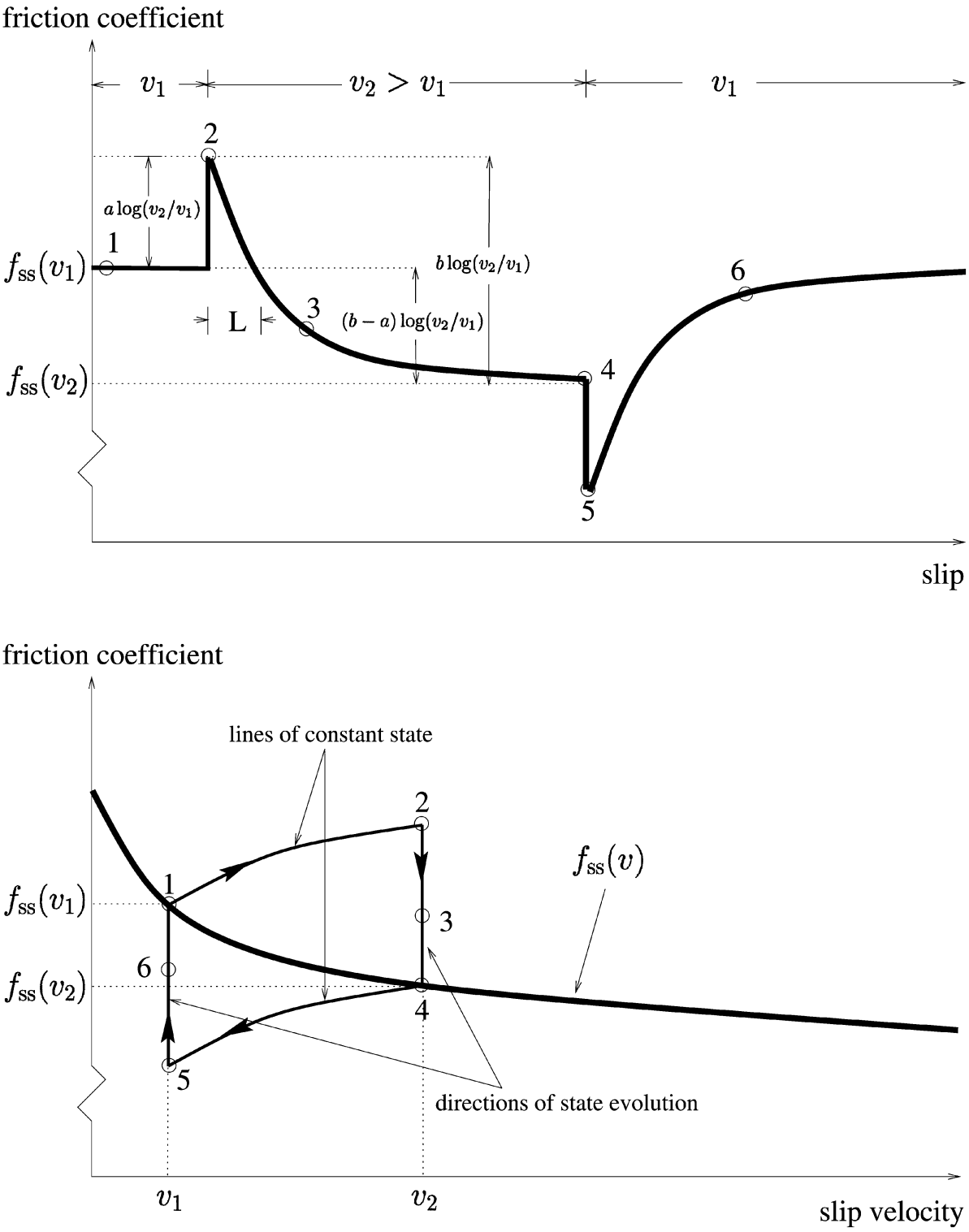

FIGURE 12 A schematic diagram illustrating the main features of rate- and state-dependent friction in laboratory experiments with sliding velocities in the range 10^{-6}–10^{-3} m/s. The top panel shows the response to velocity jumps. The bottom panel shows the steady-state frictional behavior in a velocity-weakening regime and evolution around the steady-state behavior corresponding to the velocity jumps in the top panel.

For the "slip" version (5.4c), the friction coefficient following a step change of sliding velocity from v_1 to v_2 can be written in the slip-weakening form

$$f = f_{ss}(v_2) + \exp(-\delta/L)[f_{ss}(v_1) - f_{ss}(v_2) + a\ln(v_2/v_1)] \tag{5.4e}$$

where $\delta = v_2 t$ is measured from the time of the velocity jump.

Expression (5.4a) as written is not appropriate for very low and very high values of sliding velocities. A simple regularization near $v = 0$, motivated by Arrhenius thermal activation of creep at asperity contacts, is to invert the equation to an exponential form for v and then replace $\exp(f/a)$ by $2\sinh(f/a)$. This leads to

$$f = a\sinh^{-1}\{(v/2v_0)\exp[(f_0 + b\ln(v_0\theta/L))/a]\}. \tag{5.4f}$$

In addition, v should be replaced by $|v|$ in (5.4b) and (5.4c) to allow velocity of either sign, and there should be an upper limit cutoff at some high slip velocity.

If $a > b$, the overall change of f with increasing sliding velocity is positive, the friction is velocity-strengthening, and only stable sliding is possible. On the other hand, if $a < b$, the overall change is negative, the friction is velocity-weakening, and dynamic instabilities can occur. The situation $a < b$ provides a necessary but not a sufficient condition for instability. The occurrence of instability requires a rate of weakening that is larger than the rate of stress reduction (stiffness of the system) on a slipping patch. For a given material under fixed pressure, temperature, surface roughness, and other relevant conditions, the rate of weakening is constant and is given approximately by $(b - a)\sigma_n$. The rate of stress reduction depends on the size of the zone that is slipping coherently. Infinitesimally small slip patches are infinitely stiff and are always stable, but as a slipping zone grows larger, its stiffness decreases and it can turn unstable. This happens when the slip patch reaches a critical "nucleation" size for which the rate of stress reduction is first equal (from above) to the rate of weakening. The nucleation zone size for a failure process governed by rate- and state-dependent friction is

$$h^* = C\mu L/[(b - a)\sigma_n] \tag{5.4g}$$

where C is a dimensionless constant of order 1. The nucleation size, at which there is a transition from aseismic slip to dynamic rupture, can be used to obtain an estimate for a minimum earthquake size. Observed values of L with sliding velocities in the range $(10^{-8}$–$10^{-1})$ m/s are generally somewhat smaller [13, 38] than those associated with D_c values of slip-weakening experiments. Observed values of $(b - a)$ in pressure-temperature conditions corresponding to the brittle seismogenic zone are about 0.02. The scalar potency release associated with the nucleation process can be calculated roughly by using $\mu/\sigma_n \approx 300$ to estimate h^* and multiplying the area of a circular patch with the obtained h^* by observed values of L (or D_c). Converting the result to an earthquake magnitude using empirical moment-magnitude or potency-magnitude scaling relations (see section 6) gives a range of minimum earthquake magnitude centered around -3.

6. Earthquake Source Parameters and Scaling Relations

([1], [2], [6], [8], [11], [14], [16], [19], [20], [22], [25], [26], [31], [35], [36], [39], [48], [50], [52], [53])

Faulting is associated with nonlinear inelastic deformation, intricate energy partition, evolving material properties, and other complexities. In general, faulting under natural conditions is inaccessible for direct observations, and earthquake source parameters are typically estimated from inversions of seismic and geodetic data in the far-field. This necessarily parameterizes the source process in terms of equivalent deformation in a linear elastic solid surrounding the inelastically deforming regions. Geological observations, lab studies, and measurements in mines provide limited direct information on the faulting process proper, although typically for conditions far removed from those operating in natural tectonic faults at seismogenic depths (e.g., 7.5 km for continental strike-slip faults).

The most common form of earthquake data consists of seismic catalogs that typically list the time, location, and magnitude M of earthquakes in a given space-time domain. Instead of (or in addition to) M, some catalogs list the scalar seismic moment M_0, which gives (as does the scalar potency P_0) a better physical characterization for the overall size of an earthquake source. The scalar moment and potency are typically derived from the zero-frequency asymptotes of far-field displacement spectra (see equations (3.5b) and (3.8), Fig. 7, and related results in sections 2 and 3). Additional important parameters that augment the information contained in the scalar moment and potency are radiated seismic energy E_R, stress drop $\Delta\sigma$, fracture energy G_c, rupture velocity V_r, and directivity.

With a proper distribution of stations around the fault, it is possible to derive fault-plane solutions from observed earthquake seismograms, and this has been done for many thousands of earthquakes (see equation (3.7b) and related material). Fault-plane solutions provide information on the strike, dip, and slip angles of the earthquake rupture (Fig. 13) and directions of maximum (P) and minimum (T) compressive principal stresses, with an ambiguity of an auxiliary set of quantities. Independent constraints from field observations, aftershock locations, and other information can be used, when available, to separate the earthquake fault plane and associated set of quantities from the auxiliary set. In cases of well-recorded earthquakes, seismic data can be inverted (usually with dislocation-based models) to provide detailed images of earthquake slip histories (typically so far with a resolution of about 3 km). At present, such slip models have been derived for several tens of earthquakes [36, 53].

Observed far-field displacement spectra can be fitted, after corrections to remove propagation and recording-site effects, by

$$\Omega(\omega) = P_0/[1 + (\omega/\omega_0)^{-\gamma}] \tag{6.1}$$

where P_0 is the scalar seismic potency, ω_0 is corner frequency, and observed values of the exponent γ typically fall in the range 1–3. A finite total radiated energy implies that for high-enough frequency $\gamma > 1.5$. The symbol denoting the corner frequency here is different from that used in the context of equation (3.8) because estimated values of the corner frequency obtained by fitting spectra to (6.1) differ in general from values obtained by the intersection of the low- and high-frequency spectral asymptotes. This illustrates the more general point that inferred values of seismological parameters often depend strongly on the estimation procedure.

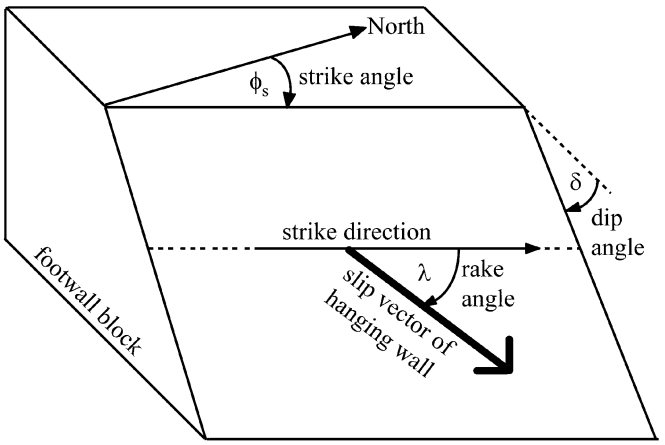

FIGURE 13 Fault and slip parameters. The strike $0 \leq \phi_s < 2\pi$ is the horizontal azimuth of the fault measured clockwise from the north. The dip $0 \leq \delta \leq \pi/2$ is the angle from the horizonal to the fault surface. The rake $-\pi \leq \lambda \leq \pi$ is the angle between the strike and slip direction of the hanging wall.

The static stress drop is defined as

$$\Delta\sigma_{static} = \sigma^0 - \sigma^f \tag{6.2a}$$

where σ^0 and σ^f are the initial and final stress values before and after the earthquake. Similarly, the dynamic stress drop may be defined as

$$\Delta\sigma_{dynamic} = \sigma^0 - \sigma^{dyn} \tag{6.2b}$$

where σ^{dyn} is a representative value of stress, such as average or minimum, during the active portion of dynamic slip (Fig. 14).

The average stress operating on the fault by the surrounding medium during an earthquake is

$$\bar{\sigma} = (\sigma^0 + \sigma^f)/2. \tag{6.2c}$$

Expression (6.2c) is usually used to denote the average stress on a fault area rather than at a point, in which case σ^0 and σ^f should be interpreted as spatial averages along the failure surface.

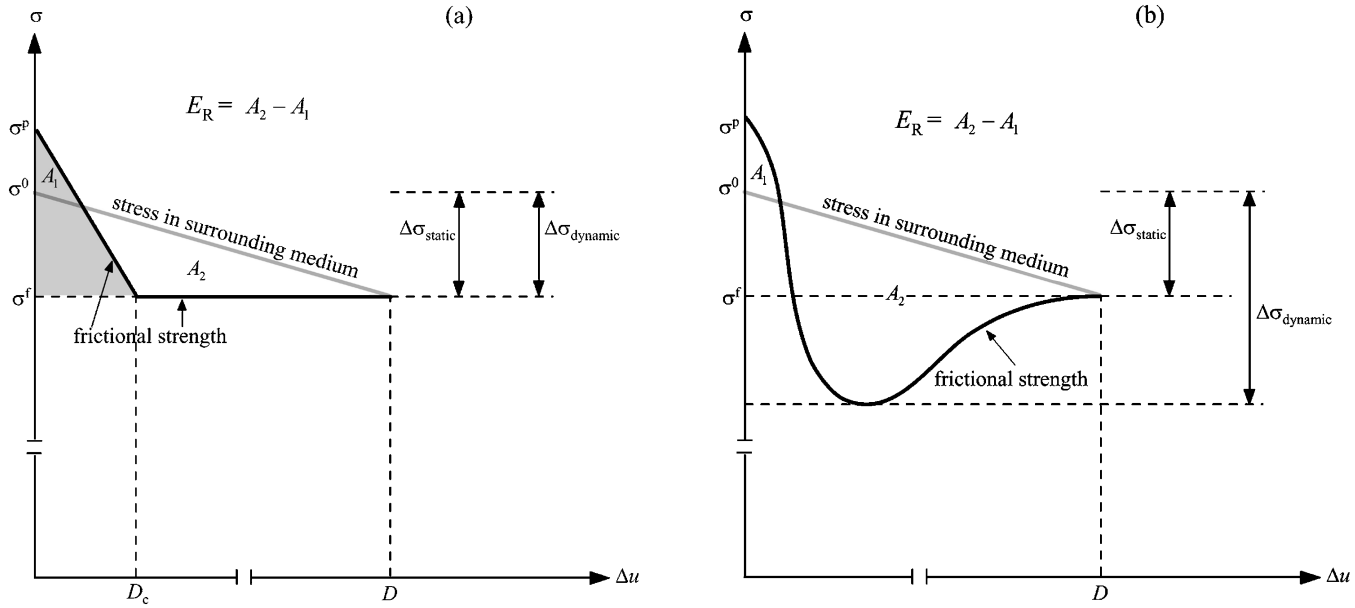

FIGURE 14 Components of energy changes associated with motion on a fault surface during an earthquake without (a) and with (b) a dynamic stress overshoot. The initial, peak, and final stress levels are denoted with σ^0, σ^p, and σ^f, respectively. The final slip is marked with D. The gray line represents the stress operating on the fault by the surrounding medium, and the black curve represents the frictional strength during slip. The radiated seismic energy E_R is the difference $A_2 - A_1$ between the areas below the gray and black lines. The area under the black curve gives the frictional heat plus fracture energy. The shaded area and D_c in (a) correspond to fracture energy G_c and critical slip-weakening distance, respectively.

The change of energy generated by an earthquake slip is

$$-\Delta E = \bar{\sigma}\ \langle \Delta u \rangle\ S = \bar{\sigma}(M_0/\mu) = \bar{\sigma}\, P_0 \tag{6.3}$$

where $\langle \Delta u \rangle$ and S are average slip and rupture area, respectively. The energy reduction in (6.3) involves changes of elastic strain energy, gravitational energy, and rotational energy of the Earth [11] and is partitioned among heat, fracture energy (which is a form of latent heat), and seismic radiation (see Fig. 14). The radiated seismic energy E_R can be estimated by integrating velocity seismograms with proper corrections for radiation pattern, attenuation, and other propagation and recording-site effects.

The apparent stress is defined as

$$\tau_a = E_R/(M_0/\mu) = E_R/P_0. \tag{6.4}$$

The seismic efficiency η is defined as

$$\eta = E_R/|\Delta E| = \tau_a/\bar{\sigma}. \tag{6.5}$$

The radiated seismic energy and surface magnitude of earthquakes in the magnitude range $5 \lesssim M_S \lesssim 8$ are related via the empirical Gutenberg-Richter relation

$$\log_{10} E_R = 1.5 M_S + 11.8 \tag{6.6}$$

where E_R is in erg (= dyne cm $= 10^{-7}$ J).

The scalar seismic moment and magnitude of earthquakes with $M \gtrsim 3.5$ are related via the empirical relation

$$\log_{10} M_0 = 1.5M + 16.1 \tag{6.7a}$$

where M_0 is in dyne cm (10^{-7} J). Empirical scaling relations between moment or potency and magnitude over a broad magnitude range with single smooth lines require a quadratic term [6, 20]. For example, the scalar seismic potency and local magnitude of California earthquakes in the range $1.0 \lesssim M_L \lesssim 7.0$ are related via the empirical quadratic relation

$$\log_{10} P_0 = 0.06 M_L^2 + 0.98 M_L - 4.87 \tag{6.7b}$$

where P_0 is in km^2 cm.

For a classical crack sustaining a uniform stress drop over a failure area S

$$M_0 = c\,\Delta\sigma_{static} S^{3/2} \tag{6.8}$$

where c is a dimensionless constant that depends on the failure geometry and elastic properties. For example, $c = 16/(7\pi^{3/2}) \approx 0.41$ for a circular crack in an infinite Poissonian solid.

For a fractal-like failure in a rough stress field [16]

$$M_0 \propto S. \tag{6.9}$$

Equation (6.8) is used often to estimate the static stress drop from inferred values of M_0 and S. The obtained values, and their physical interpretation, depend on the methods used to estimate M_0 and S. The moment is typically derived from seismograms, but sometimes it is obtained from field values or geodetic data. The area is inferred (typically with large uncertainties) from directivity effects, pulse duration, and corner frequency in seismograms (see Fig. 7, equation (6.1), and related material), as well as from aftershock locations, geological observations, and geodetic data. The corner frequency can be estimated in principle from most seismograms (although the obtained values depend strongly, as mentioned before, on the data type and estimation procedure) and, hence, is used frequently. The large uncertainties in inferred values of S produce large uncertainties in estimates of $\Delta\sigma_{static}$.

Measurements of root-mean-square acceleration in seismograms and assumptions on a source model can be used to obtain a type of dynamic stress drop that may be referred to as $\Delta\sigma_{a_{rms}}$. Another type of dynamic stress drop may be obtained from comparing the initial slope of velocity seismograms to analytical results like equation (4.6b).

Inferred values of static and dynamic stress drops averaged over the failure area are usually in the range 10^{-2}–10^2 MPa [8, 25]. Inferred average values of apparent stress typically fall in the same range, and estimates of average seismic efficiency are about 0.06 or less [39].

7. Seismicity Patterns

([9], [16], [18], [19], [23], [24], [27], [40], [56], [58], [59], [60], [62], [63])

Seismicity exhibits a wide variety of fluctuations and patterns in space, time, and energy (or magnitude) domains. At present, analysis of seismicity is largely phenomenological with little theoretical foundation, and many studies of seismicity are essentially descriptive without quantitative formulation. Examples of reported patterns include foreshocks, aftershocks, time intervals of quiescence and accelerated seismic release, changes in b values of frequency-magnitude statistics, migration of seismicity along and between faults, switching of activity on a given fault between different modes of response, and other types of spatiotemporal clustering, periodicities, and gaps. Many functions have been employed to describe statistical aspects of seismicity including power law, exponential, normal, lognormal, Gamma, Weibull, Pareto, and Cauchy distributions. Formulas and properties of these functions can be found in *http://mathworld.wolfram.com* (see also [23] and [59]).

It is important to distinguish between regional seismicity patterns characterizing large spatial domains with many faults and patterns characterizing individual fault systems. Since instrumental earthquake catalogs exist only for short duration (e.g., 50–100 y) compared to recurrence times of large earthquakes (e.g., 100–5000 y), most observational studies of seismicity have focused on regional patterns for which more data are available. Recently some works examined earthquake patterns on individual faults by combining instrumental and geological data (see, e.g., [19] and [63]). In general, regional seismicity appears to be dominated by various forms of spatiotemporal clustering, while patterns associated with large individual faults (or

fault segments) may include spatiotemporal periodicities such as quasi-periodic occurrence of system-size events and spatial regularity of microearthquake locations.

The frequency-moment statistics of regional earthquakes follow the power-law probability density function

$$n(M_0) \propto M_0^{-1-\beta} \tag{7.1a}$$

and corresponding power-law survivor function

$$N(M_0) \propto M_0^{-\beta} \tag{7.1b}$$

where $N(M_0) = \int_{M_0}^{\infty} n(M_0')\, dM_0'$.

Similar power-law relations hold for frequency-energy statistics of regional earthquakes. A maximum event size can be incorporated into (7.1a) and (7.1b) by multiplying the right sides of the equations with the exponential tapering function $\exp(-M_0/\hat{M}_0)$ having a corner moment $\hat{M}_0$ that characterizes the finite size effects. Frequency-moment distributions consisting of an initial power law for small and intermediate size events and exponential taper for large ones have been derived using several theoretical frameworks, including critical branching process, critical phase transition, and maximum entropy arguments.

Using the moment-magnitude relation (6.7a) in $n(M_0)dM_0$ of (7.1a) and $N(M_0)$ of (7.1b) leads to the discrete Gutenberg-Richter frequency-magnitude statistics

$$\log n(M) = a - bM \tag{7.2a}$$

and corresponding cumulative distribution

$$\log N(M) = A - bM \tag{7.2b}$$

where $b = 1.5\beta$ and observed b values of regional seismicity typically fall in the range 0.7–1.3. Observed frequency-moment and frequency-magnitude statistics of regional earthquakes are also analyzed with a tapered Pareto and other distributions [24, 58].

The frequency-magnitude statistics of earthquakes in large individual fault-systems, occupying narrow and long spatial domains, often consist of a Gutenberg-Richter type distribution of small events combined with enhanced statistics around a larger "characteristic" earthquake. This may be described empirically by a superposition (Fig. 15) of two separate populations, one following Gutenberg-Richter statistics over the magnitude interval $M_c < M < M_1$, and the other a Gaussian distribution centered on event size $M_2 > M_1$. Such statistics can be written as

$$\begin{aligned}\log[n(M)+1] = {} & (a - bM)H(M - M_c)H(M_1 - M) \\ & + c\exp[-(M - M_2)^2/2\sigma^2] \\ & \times H(\Delta M - |M - M_2|)\end{aligned} \tag{7.3}$$

where H is the unit step function and c is a normalization factor. If $|M_2 - M_1| > \Delta M$ as in Fig. 15, equation (7.3) has no events in the magnitude gap $M_1 < M < M_2 - \Delta M$. The distribution is assumed to describe data collected over sufficient duration so that $n + 1 \approx n$ for $M_c < M < M_1$ and $|M - M_2| <$

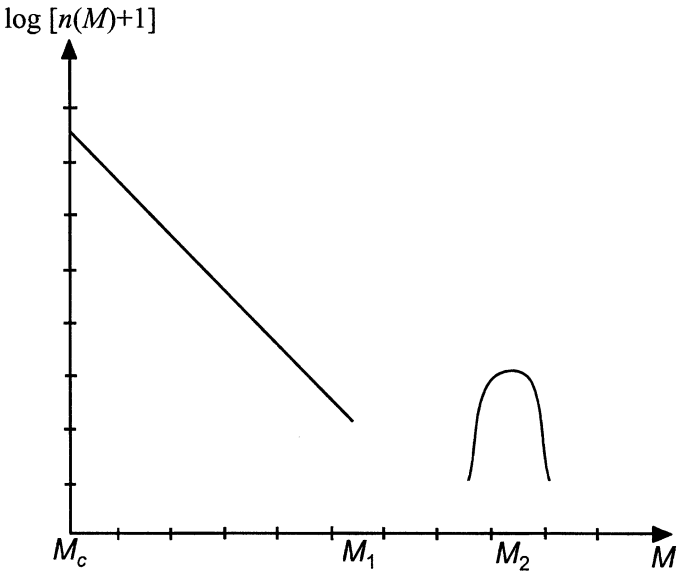

FIGURE 15 A schematic representation of discrete frequency-magnitude statistics of earthquakes on individual fault systems with two separate populations: a Gutenberg-Richter distribution of small events and a peaked Gaussian-like distribution around a large characteristic event size.

ΔM. In applications to observed data, c should be determined from the number of events associated with the "characteristic bump" around M_2 before estimating the other parameters of the Gaussian distribution. In some cases it may be possible to fix the value of M_2 based on independent geological data. It is also possible to replace the abrupt truncations in (7.3) with smooth tapering and to replace the Gaussian distribution with other peaked functions. One example is the symmetric rescaled Beta function $c(M + \Delta M - M_2)^{\alpha-1}(M_2 + \Delta M - M)^{\alpha-1}$ with $\alpha > 1$.

Aftershock decay rates can usually be described by the modified Omori law

$$\Delta N/\Delta t = K(t + c)^{-p} \tag{7.4}$$

where N is cumulative number of events, t is time after the mainshock, and observed values of the exponent p typically fall in the range 0.7–1.5. A finite total number of events implies that for large enough time $p > 1$.

The Epidemic-type Aftershock-sequences (ETAS) model combines the modified Omori law with the Gutenberg-Richter frequency-magnitude relation for a history-dependent occurrence rate of a point process in the form

$$\lambda(t|H_t) = \mu + \sum_{t_i<t} \frac{K_0 \exp[\alpha(M_i - M_c)]}{(t - t_i + c)^p} \tag{7.5}$$

where μ is a constant background rate, M_i is the magnitude of earthquake at time t_i, M_c is a lower magnitude cutoff, H_t denotes the history, and the factor $K_0 \exp[\alpha(M_i - M_c)]$ gives the number of events triggered by a parent earthquake with magnitude M_i.

Large earthquakes are sometimes preceded by a period of accelerated seismic activity in a broad surrounding region of dimension that generally scales with that of the large event. During such activation periods, several functions of various seismicity parameters (e.g., number N and moment M_0) can be fitted by a number of functional forms. One example is the power law time-to-failure relation of cumulative Benioff strain

$$\sum_{t_i<t} M_0^{1/2}(t_i) = A + B(t_f - t)^m \tag{7.6}$$

where t is time, t_f is failure time of the large event terminating the phase of accelerated seismic release, and observed values of the exponent m typically fall in the range 0.2–0.4.

Acknowledgments

The manuscript benefited greatly from many useful comments by Ralph Archuleta, Rafael Benites, Matthias Holschneider, Vladimir Lyakhovsky, Art McGarr, Takeshi Mikumo, Jim Rice, Paul Richards, Jim Savage, David Vere-Jones, Gert Zöller, and editor Willie Lee. I thank Zhigang Peng and Ory Dor for help with the text and figures preparation.

References

[1] Aki, K., and P.G. Richards (2002). *Quantitative Seismology* (second edition). University Science Books.

[2] Anderson, J.G. (2002). Strong-Motion Seismology. Chapter 57 of this Handbook.

[3] Ben-Menahem, A., and S.J. Singh (1981). *Seismic Waves and Sources*. Springer-Verlag.

[4] Ben-Zion, Y. (1989). The response of two joined quarter spaces to SH line sources located at the material discontinuity interface. *Geophys. J. Int.* **98**, 213–222.

[5] Ben-Zion, Y. (2001). Dynamic rupture in recent models of earthquake faults. *J. Mech. Phys. Solids* **49**, 2209–2244.

[6] Ben-Zion Y., and L. Zhu (2002). Potency-magnitude scaling relations for southern California earthquakes with $1.0 < M_L < 7.0$. *Geophys. J. Int.* **148**, F1–F5.

[7] Broberg, K.B. (1999). *Cracks and Fracture*. Academic Press.

[8] Brune, J.N., and W. Thatcher (2002). Strength and Energetics of Active Fault Zones. Chapter 35 of this Handbook.

[9] Bufe, C.G., and D.J. Varnes (1993). Predictive modeling of the seismic cycle of the greater San Francisco bay region. *J. Geophys. Res.* **98**, 9871–9883.

[10] Chapman, C.H. (2002). Seismic Ray Theory and Finite Frequency Extensions. Chapter 9 of this Handbook.

[11] Dahlen, F.A. (1977). The balance of energy in earthquake faulting. *Geophys. J. R. Astr. Soc* **48**, 239–261.

[12] Dahlen, F.A., and J. Tromp (1998). *Theoretical Global Seismology*. Princeton University Press.

[13] Dieterich, J.H., and B. Kilgore (1996). Implications of fault constitutive properties for earthquake prediction. *Proc. Natl. Acad. Sci. U.S.A.* **93**, 3787–3794.

[14] Feigl, K.L. (2002). Estimating Earthquake Source Parameters from Geodetic Measurements. Chapter 37 of this Handbook.

[15] Fineberg, J., and M. Marder (1999). Instability in dynamic fracture. *Phys. Reports* **313**, 1–108.

[16] Fisher, D.S., K. Dahmen, S. Ramanathan, and Y. Ben-Zion (1997). Statistics of earthquakes in simple models of heterogeneous faults. *Phys. Rev. Lett.* **78**, 4885–4888.

[17] Freund, L.B. (1990). *Dynamic Fracture Mechanics*. Cambridge University Press.

[18] Frohlich, C., and S.D. Davis (1993). Teleseismic b values; or, much ado about 1.0. *J. Geophys. Res.* **98**, 631–644.

[19] Grant, L.B. (2002). Paleoseismology. Chapter 30 of this Handbook.

[20] Hanks, T.C., and D.M. Boore (1984). Moment-magnitude relations in theory and practice. *J. Geophys. Res.* **89**, 6229–6235.

[21] Heaton, H.T., and R.E. Heaton, (1989). Static deformation from point forces and force couples located in welded elastic Poissonian half-spaces: Implications for seismic moment tensors. *Bull. Seism. Soc. Am.* **79**, 813–841.

[22] Johnston, M.J.S., and A.T. Linde (2002). Implications of Crustal Strains during Conventional, Slow, and Silent Earthquakes. Chapter 36 of this Handbook.

[23] Kagan, Y.Y. (1994). Observational evidence for earthquakes as a nonlinear dynamic process. *Physica D*. **77**, 160–192.

[24] Kagan, Y.Y. (2002). Seismic moment distribution revisited: I. Statistical results. *Geophys. J. Int.* **148**, 520–541.

[25] Kanamori, H. (1994). Mechanics of earthquakes. *Annu. Rev. Earth Planet. Sci.* **22**, 207–237.

[26] Kasahara, K. (1981). *Earthquake Mechanics*. Cambridge University Press.

[27] Kisslinger, C. (1996). Aftershocks and fault-zone properties. *Adv. Geophys.* **38**, 1–36.

[28] Kostrov, B.V., and S. Das (1988). *Principles of Earthquake Source Mechanics*. Cambridge University Press.

[29] Lawn, B. (1993). *Fracture of Brittle Solids* (2nd edition). Cambridge University Press.

[30] Lay, T., and T.C. Wallace (1995). *Modern Global Seismology*. Academic University Press.

[31] Li, V.C. (1987). Mechanics of Shear Rupture Applied to Earthquake Zones. In: *Fracture Mechanics of Rock* (B.K. Atkinson, Ed.), pp. 351–428. Academic Press.

[32] Lockner, D.A., and N.M. Beeler (2002). Rock Failure and Earthquakes. Chapter 31 of this Handbook.

[33] Lognonné, P., and E. Clévédé (2002). Normal Modes of the Earth and Planets. Chapter 10 of this Handbook.

[34] Madariaga, R. (1979). On the relation between seismic moment and stress drop in the presence of stress and strength heterogeneity. *J. Geophys. Res.* **84**, 2243–2250.

[35] Madariaga, R., and K.B. Olsen (2002). Earthquake Dynamics. Chapter 12 of this Handbook.

[36] Mai, P.M., and G.C. Beroza (2002). A spatial random field model to characterize complexity in earthquake slip. *J. Geophys. Res.*, **107**, 2308, doi:10.1029/2001/JB000588.

[37] Malvern, L.E. (1969). *Introduction to the Mechanics of a Continuous Medium*. Prentice Hall, Inc.

[38] Marone, C. (1998). Laboratory-derived friction laws and their application to seismic faulting. *Annu. Rev. Earth Planet. Sci.* **26**, 643–649.

[39] McGarr, A. (1999). On relating apparent stress to the stress causing earthquake fault slip. *J. Geophys. Res.* **104**, 3003–3011.

[40] Ogata, Y. (1999). Seismicity analysis through point-process modeling: A review. *Pure Appl. Geophys*. **155**, 471–507.

[41] Ohnaka, M. (2003). A constitutive scaling law and a unified comprehension for frictional slip failure, shear fracture of intact rock, and earthquake rupture. *J. Geophys. Res.* 108(B2), 2080, doi:10.1029/2000JB000123.

[42] Rice, J.R. (1980). The Mechanics of Earthquake Rupture. In: *Physics of the Earth's Interior* (A.M. Dziewonski and E. Boschi, Eds.), pp. 555–649. Italian Physical Society/North Holland, Amsterdam.

[43] Rice, J.R. (1993). Mechanics of Solids, section of the article "Mechanics." In: *Encyclopeadia Britannica*, 1993 printing of the 15th edition, vol. **23**, pp. 734–747 and 773.

[44] Rice, J.R. (2001). New Perspectives on Crack and Fault Dynamics. In: *Mechanics for a New Millennium* (H. Aref and J.W. Phillips, Eds.), pp. 1–23, Kluwer Academic Publications.

[45] Rice, J.R., N. Lapusta, and K. Ranjith (2001). Rate and state dependent friction and the stability of sliding between elastically deformable solids. *J. Mech. Phys. Solids* **49**, 1865–1898.

[46] Rosakis, A. (2002). Intersonic shear cracks and fault ruptures. *Advances Phys.* **51**, 1189–1257.

[47] Rudnicki, J.W. (1980). Fracture mechanics applied to the earth's crust. *Ann. Rev. Earth Planet. Sci.* **8**, 489–525.

[48] Ruff, L.J. (2002). State of Stress Within the Earth. Chapter 33 of this Handbook.

[49] Sato, H., M. Fehler, and R.-S. Wu (2002). Scattering and Attenuation of Seismic Waves in the Lithosphere. Chapter 13 of this Handbook.

[50] Scholz, C.H. (2002). *The Mechanics of Earthquakes and Faulting*. Cambridge University Press.

[51] Shearer, P. (1999). *Introduction to Seismology*. Cambridge University Press.

[52] Sibson, R.H. (2002). Geology of the Crustal Earthquake Source. Chapter 29 of this Handbook.

[53] Somerville, P.G., K. Irikura, R. Graves, S. Sawada, D.J. Wald, N. Abrahmson, Y. Iwasaki, T. Kagawa, N. Smith, and A. Kowada (1999). Characterizing crustal earthquake slip models for the prediction of strong ground motion. *Seismol. Res. Lett.* **70**, 59–80.

[54] Tada, H., P.C. Paris, and G.R. Irwin (1985). *The Stress Analysis of Cracks Handbook*, 2nd edition. Paris Productions Incorporated (and Del Research Corporation).

[55] Teisseyre, R., and E. Majewski (2002). Physics of Earthquakes. Chapter 15 of this Handbook.

[56] Turcotte, D.L., and B.D. Malamud (2002). Earthquakes as a Complex System. Chapter 14 of this Handbook.

[57] Udias, A. (2002). Theoretical Seismology: An Introduction. Chapter 8 of this Handbook.

[58] Utsu, T. (1999). Representation and analysis of the earthquake size distribution: A historical review and some new approaches. *Pure Appl. Geophys*. **155**, 509–535.

[59] Utsu, T. (2002). Statistical Features of Seismicity. Chapter 43 of this Handbook.

[60] Utsu T., Y. Ogata, and R.S. Matsu'ura (1995). The centenary of the Omori Formula for a decay law of aftershock activity. *J. Phys. Earth* **43**, 1–33.

[61] Varatharajulu, V., and Y.-H. Pao (1976). Scattering matrix for elastic waves. I. Theory. *J. Acoust. Soc. Am.* **60**, 556–566.

[62] Vere-Jones, D. (1994). Statistical Models for Earthquake Occurrence: Clusters, Cycles and Characteristic Earthquakes. In: *Proc. first US/Japan conference on the frontiers of statistical modeling: An informational approach*, pp. 105–136. Kluwer.

[63] Wesnousky, S.G. (1994). The Gutenberg-Richter or characteristic earthquake distribution, which is it? *Bull. Seismol. Soc. Amer.* **84**, 1940–1959.

[64] Wieland, E. (2002). Seismometry. Chapter 18 of this Handbook.